UNIVERSITÀ DEGLI STUDI DI MILANO

FACOLTÀ DI SCIENZE E TECNOLOGIE

CORSO DI LAUREA TRIENNALE IN FISICA

Study and performance evaluation of the FOOT experiment track reconstruction algorithm

Relatore: Prof. Franco Ersilio CAMERA

Correlatore: Dr. Yunsheng DONG

Tesi di Laurea di:
Marta OPRANDI
Matricola 957723

Anno Accademico 2021/2022

Contents

Introduction

Particle therapy is a form of radiotherapy that adopts hadrons, mainly protons and ^{12}C, to treat cancer tumors. The advantages of particle therapy with respect to conventional radiotherapy with photons are mainly given by the higher precision in the dose delivery and the better sparing of healthy tissues. As a result, at the end of 2019, a total of 222425 and 34138 patients with cancer had been treated with proton and carbon ion beams, respectively [1]. Even if particle therapy is an established method to treat different type of solid tumors, the state of the art shows different possibilities to improve the current status.

One of the research in the field of particle therapy is related to the effects of nuclear inelastic interactions. In $Z > 1$ ion therapy, projectile fragmentation can occur as a consequence of nuclear inelastic interactions. The heavy fragments produced ($Z \geq 3$) approximately have the same velocity of the projectile ion and they are emitted in the forward direction with a small angular deviation. Light fragments, instead, can be emitted even at large angles (up to about $90°$). The overall effect is a dose release outside the tumor site, with the risk of ionizing also the healthy tissues placed beyond the tumor along the beam direction. Instead, in both protontherapy and $Z > 1$ ion therapy, target fragmentation can occur leading to a non-negligible dose deposition along the beam entrance channel. These effects need to be better taken into account in the treatment planning systems to improve the quality of the treatments. Indeed, there is a lack of experimental data of nuclear differential cross sections ($\mathrm{d}^2\sigma/\mathrm{d}\Omega\cdot\mathrm{dE}$) relevant for particle therapy applications.

The FOOT (FragmentatiOn Of Target) experiment is designed to measure the differential cross sections of the fragments produced in nuclear interactions of ^{12}C, ^{16}O and ^{4}He beams impinging on targets of graphite (C), polyethylene (C_2H_4) and PMMA ($C_5O_2H_8$), at the energy range relevant for particle therapy (150-400 MeV/u) and space radioprotection (up to 800 MeV/u). The FOOT experiment data will be used as benchmark for the current MC simulation tools, improving the current nuclear interaction models and giving benefit to different fields of physics. The FOOT experiment includes two alternative setups, one with a magnetic spectrometer for the identification of fragments with $Z \geq 3$ and the other with an emulsion spectrometer for the tracking of low Z particles. The first spectrometer, which is the one taken into account in this thesis, consists of a pre target beam measurement station, a particle tracking system working in a magnetic field, a time of flight measurement system and a calorimeter.

The aim of this thesis is to evaluate the performances of the FOOT experiment track reconstruction algorithm by means of Monte Carlo simulations. Parameters such as effi-

ciency, purity, momentum and angular resolution of the reconstruction algorithm have been evaluated.

In Chapter 1 the fundamentals of charged particles interaction with matter, an overview of the nuclear interactions and particle therapy together with the involved biological aspects will be presented. Chapter 2 will illustrate the FOOT experimental setup, the aims and the strategy of measurement and the experimental requirements, followed by a description of the structure of the simulation framework and of the reconstruction algorithm based on a Kalman filter. In Chapter 3 the study of the performances of the track reconstruction algorithm is presented: efficiency, purity, momentum and angular resolution have been evaluated.

CHAPTER 1

Nuclear Physics and Biology

1.1 Introduction

Medical physics is one of the applications emerged in the last century in the framework of interaction of radiation with matter. In particular, one of its scientific research fields is Particle Therapy (PT). The purpose of PT is to treat cancer tumors with charged hadrons, exploiting their physical properties in the interaction with matter and the biological response of the irradiated tissues. Protons and ^{12}C are the main particles currently employed in PT. The advantages in the use of hadrons with respect to photons in tumor treatments are mainly given by the higher precision in the dose delivery and the better sparing of healthy tissues.

The fundamentals of charged particles interaction with matter are presented in Sec.1.2, while in Sec.1.3 an overview of PT is shown. Nuclear interactions and their role in PT are presented in Sec.1.4.

1.2 Interaction of charged particles with matter

The interaction of charged particles with matter is mostly governed by Coulomb forces acting between the incident particle and the orbital electrons of an absorbing medium. Although with lower probability, interaction with nuclei, which is also relevant in PT, may occur. Charged hadrons, which are of interest in PT, must be considered separately from electrons because of the large difference in their masses that significantly affects the scattering and the magnitude of the energy transfer in collisions. A charged particle interacts with nearly every atom along its path, losing energy each time in atomic excitation and ionization.

There are four main types of interaction of charge particles with an atom, depending on the size of the classical impact parameter b of the charged particle trajectory compared to the classical atomic radius r_a of the absorber atom with which the charged particle interacts [2]:

- **Inelastic collision with atomic electron**: the particle interacts with a single atomic electron which gets ejected generating a δ-ray ($\sim$ MeV) (hard or close collision, $b \approx r_a$) or, most likely, with the atom as a whole transferring a very small amount of energy ($\sim$ eV) (soft or distant collision, $b \gg r_a$). In the latter case, the atom can be excited to a higher energy level or ionized by ejection of a valence electron.

- **Elastic interaction**: the incident particle is scattered by the target nucleus modifying the initial direction, but without changing the kinetic energy ($b \ll r_a$).

- **Inelastic radiative interaction**: this phenomenon is known as bremsstrahlung: a charged particle arriving in the vicinity of an atom will be affected by the electromagnetic field produced by the electrons of this atom. Because of this interaction, the particle will emit photons which will reduce its energy. The bremsstrahlung radiation is relevant only for light particles such as electrons or positrons. It depends on the atomic number and the atomic mass of the target medium.

- **Inelastic nuclear interaction**: an inelastic nucleus-nucleus collision does not conserve the kinetic energy and it can lead to the fragmentation of the projectile and/or of the target nucleus, leading to the generation of new particles.

1.2.1 Stopping power

The interactions described in Sec.1.2 contribute together to the stopping power S which is defined as the rate of energy loss dE per unit of path length dx of a charged particle in an absorbing medium and which depends on the characteristic of the particle as well as the absorber [2].

With regard to charged particles interactions, different types of stopping power must be considered: electronic S_{el}, radiative S_{rad} and nuclear S_{nucl}.
The latter is related to elastic collisions, but contributes to the total stopping power only for heavy particles impinging on light absorber because the energy transferred to the atom is proportional to the ratio of the mass of the incident particle to the mass of the target atom. The S_{nucl} starts to become relevant when the energy of the incident particle slows down under 10 KeV/u. The S_{rad} term, related to inelastic radiative interactions, can be significant for light particles (e.g. electrons), but, for heavy particles, it is negligible in comparison with the S_{el} term. The S_{el}, the electronic (or collisional) stopping power, is related to inelastic collisions and, for hadrons, is the term which most contribute to the total stopping power.

The first formulation of the stopping power is given by Niels Bohr (1913), who followed a classical approach based on the concept of impact parameter between the particle's trajectory and the absorber nucleus [3]. However, the comparison with experimental data shows that Bohr classical theory does not provide a realistic description of particles stopping in absorbing media, especially at energies where relativistic effects need to be considered (e.g. energies comparable to the rest mass of the charged particle).

A good agreement between theoretical and experimental data was achieved by the stopping power theory based on quantum mechanical and relativistic concepts developed by Bethe and Bloch (1931) [3]:

$$S = -\frac{dE}{dx} = 2\pi\, N_a\, r_e^2\, m_e\, c^2\, \rho\, \frac{Z}{A}\, \frac{z^2}{\beta^2} \left[\ln\left(\frac{2 m_e\, \gamma^2\, v^2\, W_{max}}{I^2} \right) - 2\,\beta^2 - \delta - 2\,\frac{C}{Z} \right] \qquad (1.1)$$

where N_a is the Avogadro constant; r_e and m_e are respectively the classical radius and the mass of the electron; ρ, Z and A respectively denote density, atomic number and atomic weight of the absorbing medium and z is the charge of the incident particle. W_{max} is the maximum kinetic energy that can be transferred to an electron of the medium in a single collision. I is the mean ionization/excitation energy that accounts for all possible atomic ionizations as well as atomic excitations and it can be determined empirically. A useful approximation of the mean excitation energy is given by [4]:

$$\mathrm{I} = \begin{cases} 12\,\mathrm{Z} + 7 & \text{eV if } Z \leq 13 \\ 9.76\,\mathrm{Z} + 58.8\,\mathrm{Z}^{-0.19} & \text{eV if } Z > 13 \end{cases}$$

It is important to note that I only depends on the absorbing medium and that it increases with increasing the atomic number Z.

The Bethe-Bloch formula is an extension of the Bohr one in which the following corrections are introduced:

- Shell correction (C/Z) and effective charge (Z_{eff})
- Density (polarization) effect (δ)

Eq. 1.1 is valid for particles with $0.05 \leq \beta\gamma \leq 500$ and mass equal or heavier than the muon ($\simeq 100$ MeV$/c^2$). So, Bohr formulation assumes that the velocity of charged hadrons is much larger than the velocity of the bound orbital electrons of the absorber. Nevertheless, at low kinetic energy (~ 1 MeV) this assumption fails because orbital electrons stop participating in energy transfer from the charged particle when their velocity becomes comparable to the charged particle velocity. The shell correction term (C/Z), which is a function of the absorbing medium and of the charged particle velocity, is then introduced to compensate the overestimation of the atomic number Z (and of the I value as a consequence). Another correction needed at low kinetic energies involves the charge z of hadrons: travelling through the medium, the incident particles lose their energy (and momentum) and they can capture electrons causing a decrease of their charge. Since in Eq.(1.1) there is a z^2 dependence, the electron capture leads to an energy loss lower than the one expected. To consider this effect, W.H. Barkas [5] introduced an effective charge

$$Z_{eff} = Z[1 - \exp(-125\,\beta\, Z^{-2/3})] \tag{1.2}$$

to replace the z term for particles with energies below 1 MeV/u. This low kinetic energy region can be observed in Fig.1.1 which shows an example of stopping power as a function of momentum p.

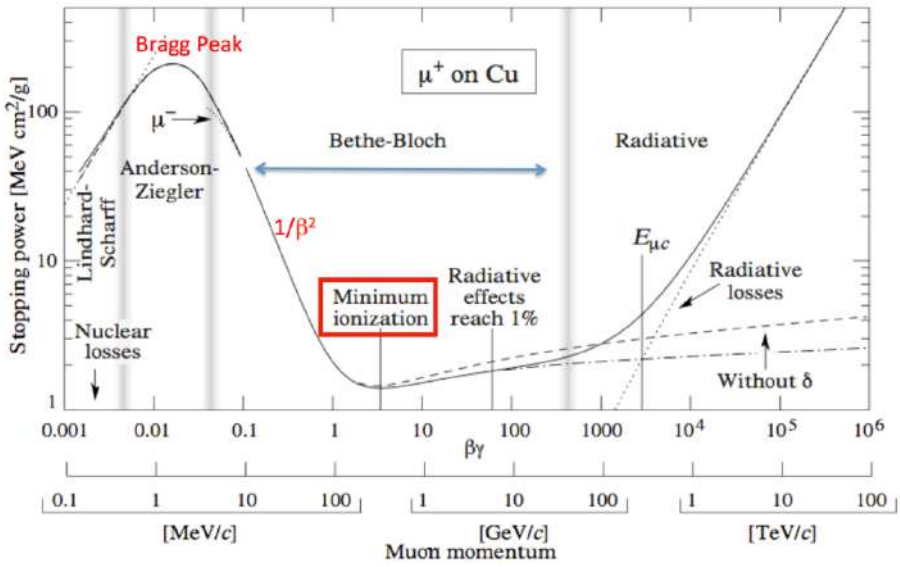

Figure 1.1: Stopping power for positive muons in copper as a function of momentum p [6].

Instead, the correction for density effect is important at relativistic energies and is needed because hadrons interact with more than one atom at a time in the medium.

Therefore, the dipole distortion of the atoms near the particle track weakens the Coulomb force field experienced by the more distant atoms, thus decreasing the energy transferred to them. This relativistic energy region is shown in Fig.1.1: it is characterized by a slow rise of the stopping power with increasing the kinetic energy as a result of the relativistic term $ln\gamma^2 v^2 - 2\beta^2$.

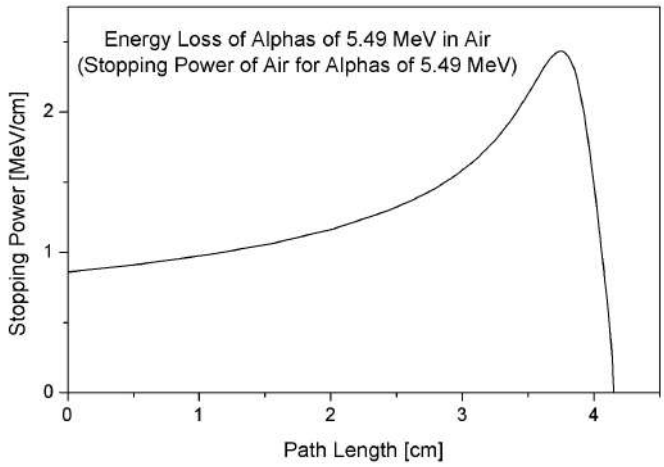

Figure 1.2: Bragg curve [7].

The peak depicted in Fig.1.1 is the Bragg peak: dE/dx increases when the charged particle loses its speed while travelling through the absorbing medium. At the end of its trajectory, the particle transfers a large amount of energy in proximity of any material electron. Then, it starts to pick up the electrons, lowering its effective charge and the stopping power drops, resulting in that peak (also shown in Fig.1.2).

Except at low energies, a given absorbing material will have the same stopping power for all hadrons of a given velocity and charge because S_{el} does not depend on the mass of the heavy charged particle.

The dependence of the Bethe-Bloch formula on the absorbing medium is given by the density, the ratio Z/A and the mean ionization energy I. Since the density of the medium weighs on the final value of the stopping power, the mass stopping power $S = \frac{1}{\rho}\frac{dE}{dx}$ can be defined to remove the material dependence also thanks to the ratio Z/A which is almost constant (it varies from 0.5 to 0.4 from low to high Z elements). This allows a comparison between different materials on a smaller scale enhancing the other dependencies (e.g. Fig.1.1).

1.2.2 Range and energy straggling

The path length of a particle that travels inside a medium until it loses its energy and comes to rest is defined as the range.

In principle, the theoretical value of the range is different from the measured one, which is the thickness of an absorbing medium that a particle can penetrate. The differences between the theoretical and the measured range are negligible for hadrons at the energies involved in PT.

The range can be obtained as:

$$R(E_0) = \int_0^{E_0} \left(\frac{dE}{dx}\right)^{-1} dE \tag{1.3}$$

where E_0 is the initial kinetic energy of the charged particle. This is the continuous slowing down approximation (CSDA) range: a quantity that represents the average path length travelled by a charged particle as it slows down to rest. In this approximation, the rate of energy loss at every point along the track is assumed to be equal to the total stopping power, neglecting the energy-loss fluctuations.

The determination of the CSDA range can be computed by solving the integral in Eq. (1.3) or by using different approximations such as the Bragg-Kleeman rule [8]:

$$R(E_0) \sim \alpha E_0^p \tag{1.4}$$

For protons of therapeutic energies (E_0 between 50 and 250 MeV) p $\approx$ 1.7 - 1.8. Since E_0 is given in MeV and $R(E_0)$ in cm, the dimension of α is cm/MeV^p. A precise knowledge of p requires a comparison with the solution of Eq. (1.3) or with Monte Carlo calculations.

The dE/dx is a stochastic process: in each interaction different amount of kinetic energy can be transferred to atomic electrons. Then, the energy loss has a distribution function:

- For thin layers or low density materials the incident charged particle experiences few collisions, some with high energy transfer. The energy loss distribution is asymmetric, showing a long tail towards high values of energy loss. This effect is the energy straggling. A possible parametrization is given by the Landau function:
$$f(\lambda) = \frac{1}{\sqrt{2\pi}} \exp\left(-\frac{1}{2}(\lambda + e^{-\lambda})\right) \tag{1.5}$$
where λ depends on the energy loss and on the absorber's parameters (Z, A etc.). An example of Landau distribution is shown in Fig.1.3.
The energy loss distribution is not Gaussian around mean because in some cases a lot of energy is transferred to a single electron producing δ rays.

- For thick layers and high density materials the charged particle undergoes many collisions and the energy distribution function get Gaussian shaped. Assuming that the particle loses ΔE energy in a Δx step in the material, the parametrization is given by [9]:
$$F(\Delta E) = \frac{1}{\sqrt{2\pi\sigma}} \exp\left(\frac{\Delta E - \langle \Delta E \rangle}{2\sigma^2}\right) \tag{1.6}$$
In this case, the energy distribution function is Gaussian as a consequence of the central limit theorem and its width depends both on material and projectile:
$$\sigma^2 = 4\,\pi\, Z_{eff}^2\, Z\, e^4\, N_A\, \Delta x \left(\frac{1 - \beta^2/2}{1 - \beta^2}\right) \tag{1.7}$$

The energy loss straggling leads to the range straggling [3] which is shown in Fig.1.4: experimentally, the range can be determined by passing a beam of particles at the desired energy through different thicknesses of the absorbing medium and measuring the ratio of transmitted I to incident particles I_0. The fact that the curve slopes down over a certain spread of thicknesses is because the energy loss is not continuous, but statistical in nature.

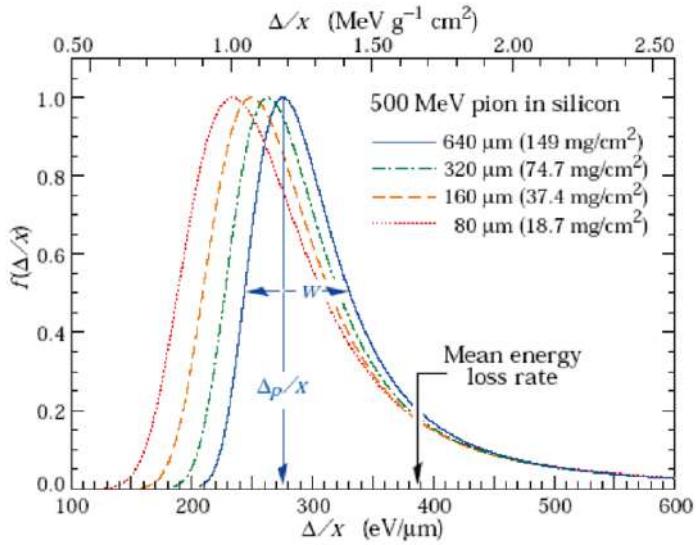

Figure 1.3: Example of Landau distribution for 500 MeV pions incident a thin Silicon detector for different value of thickness. w is the full width at half maximum [6].

1.2.3 Multiple Coulomb Scattering

As presented in section 1.2, charged particles that undergo elastic collisions with target nuclei are scattered and the result of the interaction is a deviation of the incoming particles direction of motion without kinetic energy loss.

When the thickness of the target is small, the probability of having more than one interaction is negligible [3]: this type of scattering is described by the Rutherford formula, which is based on the assumption that the energy of the incident particle is conserved during the scattering process:

$$\frac{d\sigma_R}{d\Omega} = \left(\frac{zZe^2}{pv}\right)^2 \frac{1}{4\sin^4(\theta/2)} \tag{1.8}$$

The Rutherford cross section takes into account the charge of the incident particle and of the target (z and Z respectively) and the angle of scattering. Because of the $1/\sin^4(\theta/2)$ term, the majority of the collisions result in a small angular deflection of the particle.

However, with increasing the thickness of the absorbing medium, the number of interactions increases resulting in a Multiple Coulomb Scattering (MCS) process. Even if the consequence of an interaction between the charged particle and the medium is a small change in the incident particle direction, all the scattering contributions can lead to a non negligible deviation of the projectile from the initial trajectory and the statistical outcome is a deflection angle whose distribution is approximately Gaussian [10]. This process is well described by Molière's theory [11].

For small angles, the angular distribution can be approximated by a Gaussian with a standard deviation σ given by Highland [12]:

$$\sigma_\theta = \frac{14.1\,\text{MeV}}{\beta\, p\, c}\, z\sqrt{\frac{d}{X_0}}\left[1 + \frac{1}{9}\log_{10}\left(\frac{d}{X_0}\right)\right] \tag{1.9}$$

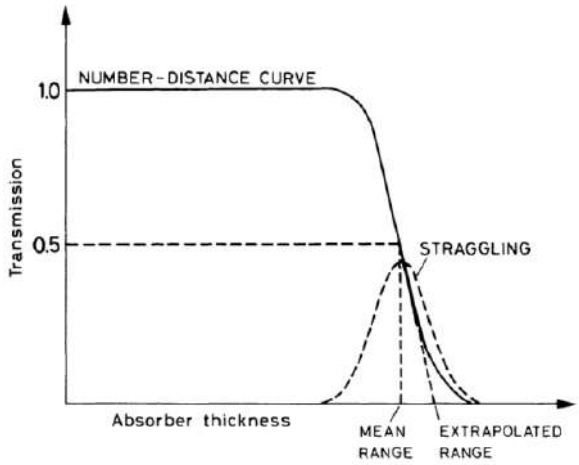

Figure 1.4: Behavior of the ratio I/I_0 as a function of the absorber thickness. The CSDA range is the distance where $I = I_0/2$ [3].

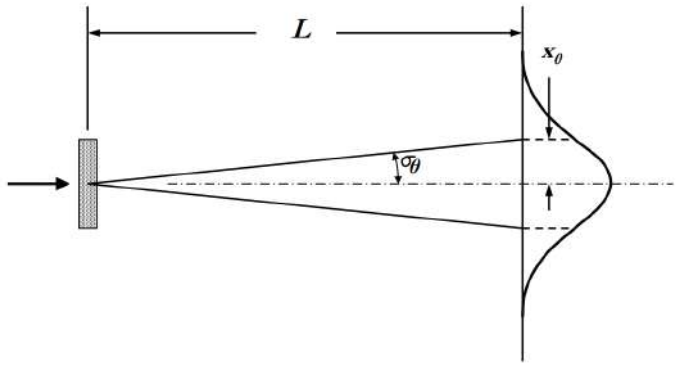

Figure 1.5: Gaussian projected displacement in a measuring plane. σ_θ is the width of the angular distribution and X_0 is the corresponding displacement [10].

where p, β and z are respectively momentum, velocity and charge of the incident particle and d/X_0 is the absorber material thickness in units of radiation length, which is the mean length (in cm) to reduce the energy of an electron by the factor $1/e$. The latter can be approximated by the following analytical formula:

$$X_0 = \frac{716.4}{Z(Z+1)\ln\frac{287}{\sqrt{Z}}}\ g/cm^{-3} \tag{1.10}$$

where the result in cm can be obtained dividing by the density. Values of radiation length for different materials are measured and collected in databases [13].

For compounds and mixture, the radiation length can be estimated as:

$$\frac{W_0}{X_0} = \sum_i \frac{W_i}{X_i} \tag{1.11}$$

where W_0 is the total mass of the sample, W_i and X_i are respectively the mass (fraction by weight) and the radiation length of the i-th component (for water $W_0 = 36g/cm^2$).

Considering the same material thickness, materials with large Z cause more scattering: $X_0 \sim 1/z^2$

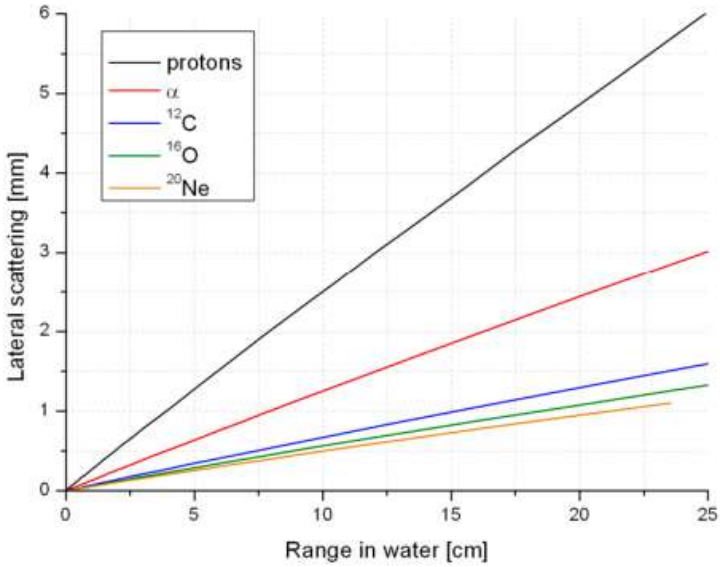

Figure 1.6: Charged particle beam widening in water for different particle beams as a function of range, obtained through a Monte Carlo simulation [14].

Moreover, the angular spread for the same range is smaller for heavy particles: equation (1.9) results in a larger transverse widening for protons with respect to carbon ions, as illustrated in Fig.1.6. For example, comparing protons and carbon ions beams respectively at the energies of 150 MeV and 285 MeV, at 15.6 cm depth, the spread is approximately three times larger for protons:

$$\left(\frac{Z_p}{\beta pc}\right)_p \approx 3\left(\frac{Z_p}{\beta pc}\right)_{^{12}C} \tag{1.12}$$

However, the angular spread increases for hadrons at low energies, due to the βcp term of Eq.(1.9).

Fig.1.7 shows a limit in the Highland approximation: the angular spread of a proton beam of 158.6 MeV interacting with water is Gaussian shaped and the Molière distribution is indistinguishable from the one obtained with the Highland formula if the angular spread is up to 2.5 sigma. At higher values, the Highland approximation underestimates the MCS effect.

Corrections to the distributions [15, 16] are needed only if nuclear interactions that can produce large angles deviations need to be taken into account. However, the Highland formulation of Eq.(1.9) is enough accurate for radiotherapy purposes.

The calculation of MCS angles by means of Monte Carlo (MC) simulations is crucial for the computation of absorbed dose distributions performed by treatment planning

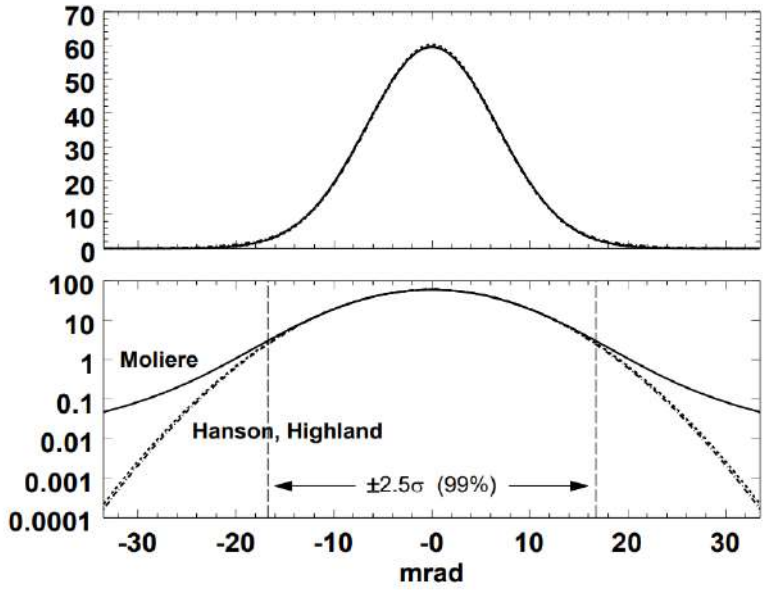

Figure 1.7: Angular distribution of a proton beam of 158.6 MeV [10].

system (TPS). An algorithm which is an approximation to the analytic description of Molière and Highland theories has been developed [17] to include the effects of MCS and to provide proper treatment of large angles (beyond the region of validity for the small angle approximation) allowing the fast generation of random scattering angles as needed for MC simulations.

1.3 Particle Therapy

Particle therapy (PT) with protons or heavier ions like ^{12}C has been introduced in radiotherapy to exploit the properties of hadrons for the treatment of solid tumors. The main advantages of PT with respect to the conventional radiotherapy conducted with photons are an improved dose delivery accuracy, an enhanced radiobiological effectiveness and a reduction of acute and long-term side effects caused by ionizing radiation deposition in normal tissues surrounding cancer cells. Currently, protons and carbon ions are the main particles employed in PT. However, helium ions beam therapy is an emerging modality for hadrontherapy and it is under study the possibility to use also oxygen beams as an additional alternative [18].

In order to study the advantages of PT with respect to conventional radiotherapy, different biological parameters are presented in the following section.

1.3.1 Biological parameters

Dose
The absorbed dose is the quantity which describes the absorption of energy in a medium. It is given by the ratio dE over dm, where dE is the mean energy imparted by ionizing

radiation to matter of mass dm:

$$D = \frac{dE}{dm} \tag{1.13}$$

The dose is measured in Gray ($1Gy = 1J/Kg$) and, for a given dose, different types of ionizing radiations produce different biological effects as well as different tissues have different radiosensitivity.

Linear Energy Transfer
The Linear Energy Transfer (LET) is defined as the energy dE released per unit length dx by the ionizing radiation traversing the material:

$$\text{LET}_\Delta = \frac{dE_\Delta}{dx} \tag{1.14}$$

The LET is expressed in terms of KeV/μm or MeV/cm. It differs from the stopping power because the latter is defined as the energy loss of the particle while the LET is defined with the energy transferred to the material surrounding the particle track. The Δ shown in Eq.1.14 is an upper energy threshold to exclude secondary electrons with high energy. If the upper limit is not considered, the LET_∞ corresponds to the electronic stopping power.

Relative Biological Effectiveness
Different types of ionizing radiations can produce very different biological effects on the same target tissue. Since the dose and the LET are not sufficient to fully take into account this effect, the Relative Biological Effectiveness (RBE) has been introduced in the clinical practice. The RBE is defined as the ratio between a reference radiation dose D_{ref} (usually $^{60}Co\,\gamma$ rays) and the dose of the radiation of interest D_{ion} that gives the same biological effect (isoeffect):

$$\text{RBE} = \left.\frac{\text{D}_{\text{ref}}}{\text{D}_{\text{test}}}\right|_{\text{iso}} \tag{1.15}$$

The RBE depends on different parameters such as the type of the target cells, their oxygenation level, the dose and the incident particle species. The dependence of RBE on LET for charged particles is shown in Fig.1.8. The RBE increases with increasing LET up to about 100-200 KeV/μm and then decreases because of overkilling effect [19]. The RBE is a fundamental parameter to develop a PT treatment. Typical RBE values for the particles involved in PT are of the order of 1.5-5 for ^{12}C ions, depending on the particle energy and LET. Instead, in clinical practice, protons have a fixed RBE value of 1.1.

1.3.2 Comparison between PT and conventional radiotherapy

As illustrated in section 1.2.1, projectile hadrons interact with the target material atoms mainly through collisional processes and they have the highest energy transfer at the end of their track. Therefore, the incident beam dose profile is characterized by the presence of a flat plateau in the beam entrance region, followed by the Bragg peak where the energy release of the particles is much more relevant. Photons energy release, on the other hand, is characterized by an exponential attenuation with increasing depth beyond the peak dose placed at the first few centimeters of the entrance channel. Thus, photons continue to deposit their energy in normal tissues beyond the tumor, exposing and potentially damaging the healthy tissues surrounding the tumor volume [21]. The depth-dose profile of photons and hadrons is shown in Fig.1.9.

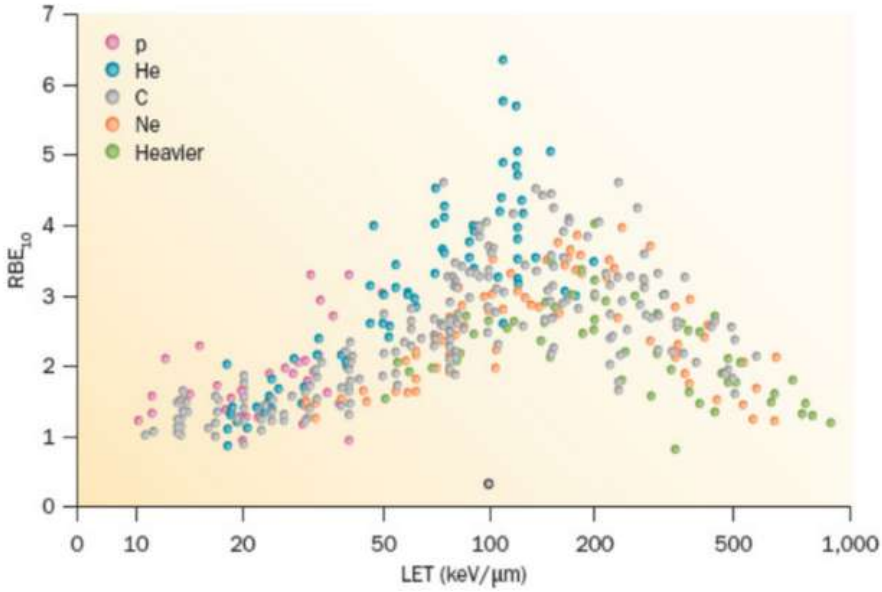

Figure 1.8: RBE against LET from protons to heavy ions [20].

The precise dose conformation to the tumor volume that can be achieved with PT allows to treat tumors localized in proximity of Organs At Risk (OARs, e.g. heart and brain), such as ocular melanomas. Due to the Bragg peak, hadrons can be used instead of photons to deliver the same dose to the target volume, reducing the exposure of healthy tissues close to the tumor site [22]. This property of PT is relevant especially for the treatment of tumors in pediatric patients.

Since the Bragg peak is narrow with respect to the usual tumor depth and its location depends on the beam energy, in clinical practice beams with the same direction and different energies are applied onto the patient in order to cover the tumor volume depth. The uniform dose distribution thus obtained in the depth-dose profile is called Spread Out Bragg Peak (SOBP) and it is shown in Fig.1.10.

Another comparison between PT and conventional radiotherapy concerns the LET, which directly affects the relevance of the DNA damages that can be caused by ionizing radiation. Photons adopted in conventional radiotherapy are considered as low LET particles. On the contrary, heavy charged particles adopted in PT are considered as high LET ones. Some tumors, especially hypoxic ones, are radioresistant to low LET radiation, for this reason they can be more efficiently treated with carbon ions. Moreover, the dose released at the entrance of the medium needs to be checked: when treating deep tumors through long entrance channels, a beam with the lower RBE possible at the entrance and a high RBE in the SOBP has to be employed. ^{12}C ions meet this requirement.

Despite the benefits of PT in terms of sparing of healthy tissues and enhancement of radiobiological effectiveness, PT cannot be adopted in the treatment of non-solid or diffused tumors. The costs of PT centers are much higher with respect to the conventional radiotherapy centers due to the different type of accelerators adopted to deliver the incident beam.

Even if PT is an established radiotherapy technique adopted in different part of the world, there is still room for improvements. As an example, the impact of nuclear inelas-

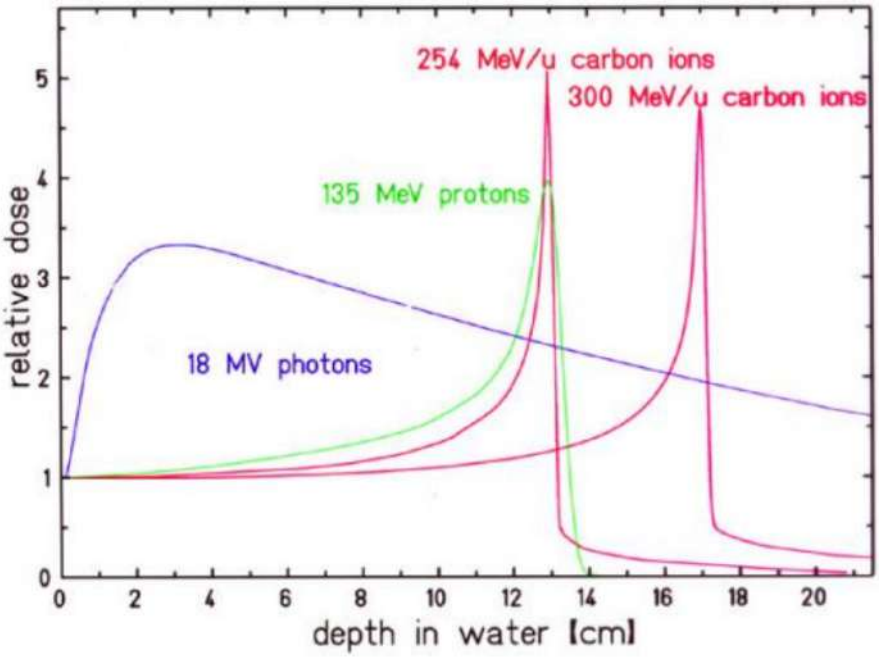

Figure 1.9: Depth-Dose profile of photons, protons and carbon ions crossing water [20].

tic interactions in the dose calculation of the Treatment Planning Systems (TPS) is still under study.

1.4 Nuclear Interactions of interest for PT

In general, there are two kinds of nuclear reactions: elastic and non-elastic. Elastic interactions do not change the internal structure of the projectile and of the target and do not produce new particles. Their effect is to transfer part of the projectile energy to the target (lab system), or equivalent to deflect in opposite directions target and projectile (center-of-mass system (CMS)) with no change in their energy. There is no threshold for elastic interactions. Instead, non-elastic reactions are those where the internal structure of the projectile and/or of the target is changed and new particles can be produced. A specific non-elastic reaction has usually an energy threshold below which the reaction cannot occur.

If the projectile is a proton, the interaction process is outlined in Fig.1.11: there are four time and energy dependent stages. The Intra-Nuclear Cascade (INC) is the first one: the projectile hits the nucleus (collision with the target nucleons). The product of this interaction can hit other neutrons and protons and so on. The most energetic particles (protons, neutrons, γ rays) and a few light fragments are emitted in this phase and new particles are produced if the energy is above a certain threshold. So, primary particles can be re-scattered and they may produce secondary particles or they escape from the target. The INC stage ends below 50 MeV, which is the cut-off energy where the particles are considered to be absorbed by the nucleus. Then, the second stage, pre-equilibrium, starts: the remaining excitation energy is partitioned among the nucleons through a chain of collisions. This step can be described by Blann's model [25]. The

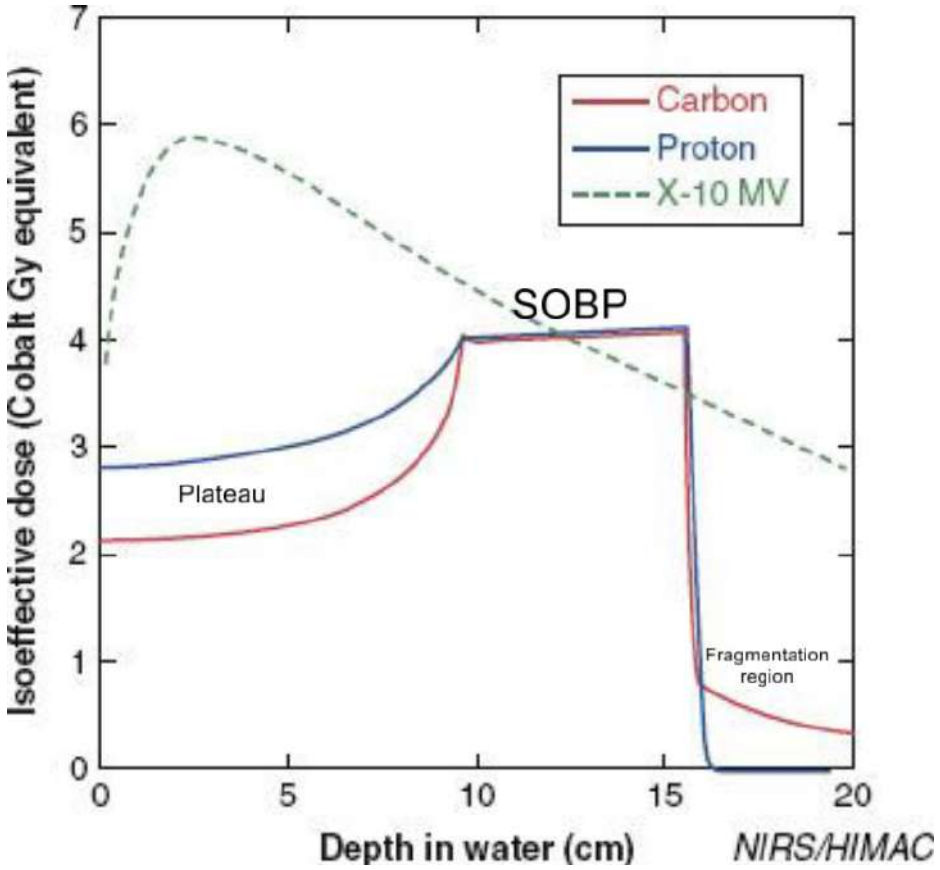

Figure 1.10: Spread Out Bragg Peak of different beam in water [23].

chain ends when the excitation energy decreases below the threshold of light fragments emission. After many collisions and possibly particle emissions, the residual nucleus is left in a highly excited "equilibrated" state. De-excitation can occur by nuclear evaporation, where light particles of low energies ($\sim$ MeV) are emitted, or by fission in the case of heavy nuclei, where the excitation energy can be large enough to allow breaking into two major chunks. Both processes are described by statistical models [26, 27]. Finally, the residual nucleus may de-excite through γ rays emission.

If the incoming particle is a heavy ion, the interaction process is described by models which start from the nucleons-nucleus interaction of Fig.1.11 and extend it to the nucleus-nucleus one [28, 29].

1.4.1 Projectile and Target Fragmentation in Particle Therapy

As mentioned in Sec.1.4, projectile and target fragmentation can occur in nuclear inelastic interactions. In particular, unlike in protontherapy, where only target nuclei fragmentation can occur, in $Z > 1$ ion therapy also projectile fragmentation can happen. For this reason, protons have no exit dose beyond the Bragg peak, while for heavier ions, additional nuclear fragmentation processes lead to a fragment tail in the depth-dose profile contributing to the dose delivery.

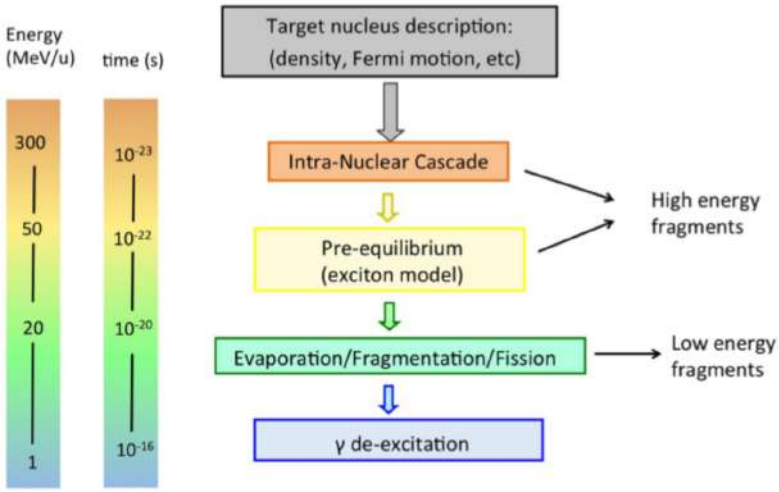

Figure 1.11: Simplified scheme of nucleons-nucleus interaction [24].

Projectile fragmentation
The heavy fragments produced in nuclear interactions approximately have the same velocity of the ion projectile and they are well collimated in the forward direction. Light fragments, instead, are emitted mostly at large angles (up to $90°$). The overall effect is a dose release beyond the Bragg peak given by fragments produced by secondary particles (the primary ions stop in the peak). The main contribution of the secondaries is given by proton and helium particles that lead to a long dose deposition tail beyond the Bragg peak [30].

Target fragmentation
The fragmentation of the target nuclei occurs both in protontherapy and in heavy ion therapy. The secondary particles are produced along the beam direction from the entrance channel to the Bragg peak. Target fragments are difficult to detect because they have low energies ($\sim$ MeV) and short ranges ($\sim \mu$m). A study performed with MC simulations [31] enhances the relevance of target fragments dose deposition ahead of the Bragg peak, showing the necessity to improve the nuclear models currently employed in the clinical TPS.

Fig.1.12 schematically shows the impact of ionization and target fragmentation in tissue sections of 1×1 mm^2. Close to the Bragg peak the biological effect is mainly due to ionization events, while in the entrance channel the target fragmentation plays a significant role.

Both projectile and target fragmentation should be better considered in the TPS simulations in order to estimate the whole dose deposition correctly. More experimental data are necessary to study the nuclear interaction models and to improve MC simulation codes and current TPS: new measurements of the fragmentation cross sections of particles at the energies involved in PT are required [32].

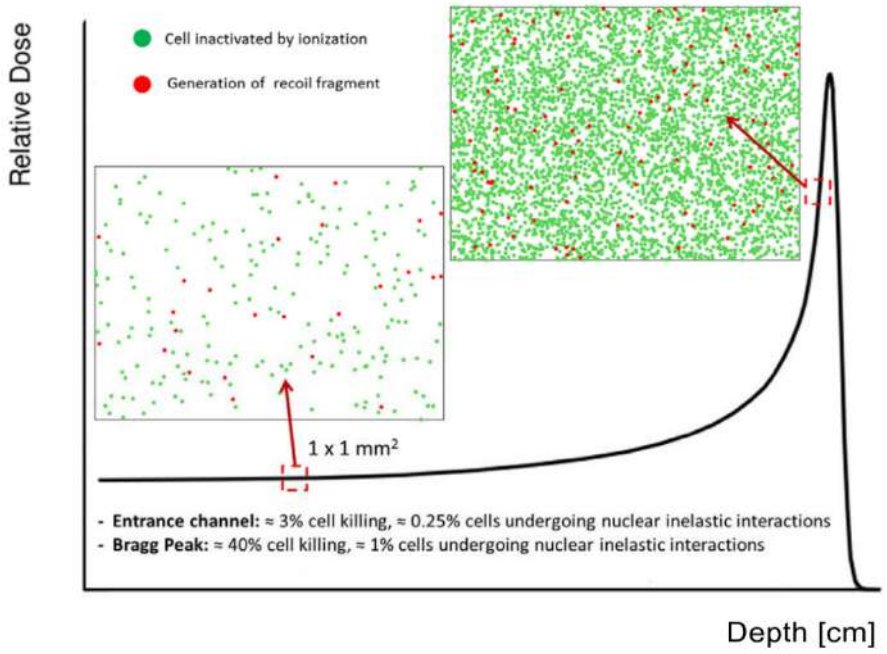

Figure 1.12: Plot of cells killed by primary ionization (green) and fragmentation effect (red) [31].

CHAPTER 2

The FOOT Experiment

2.1 Introduction

The FOOT (FragmentatiOn Of Target) collaboration designed an experiment to study the nuclear fragmentation interactions of H, ^4He, ^{12}C and ^{16}O ions of interest for Particle Therapy (PT) and Radiation Protection in Space (RPS). Since nuclear fragmentation plays an important role in these applications and due to a lack of experimental data, the FOOT project has the purpose of performing precise measurements of differential fragmentation cross sections, with respect to the emitted fragment kinetic energy and production angle, in the energy range of interest for PT and RPS [33]. The particle species currently available in PT (protons and ^{12}C) or the alternative candidates under study (^4He and ^{16}O) are also present in the galactic Cosmic Rays which are one of the main causes of radiobiological damage for astronauts involved in long term and far from Earth space missions. Also in the framework of space radioprotection there is a lack of cross section measurements that are required to benchmark the current Monte Carlo (MC) simulation tools and to design a proper shielding material suitable for the future space missions. Details about the aims and the strategy of measurement are presented in Sec.2.2. The experimental setup is illustrated in Sec.2.3 and the experimental requirements in Sec.2.4. The FLUKA MC simulation tool has been adopted for the simulation of the FOOT apparatus and to perform preliminary performance studies. A description of the simulation code together with its output is presented in Sec.2.5. The last section, Sec.2.6, describes the reconstruction software developed within the FOOT experiment that has been employed in this thesis to perform the analysis on MC simulations.

2.2 Aims and strategy of measurement

The FOOT experiment was funded by INFN (Istituto Nazionale di Fisica Nucleare, Italy) in 2017 and it is composed of researchers from France, Germany, Italy, Japan and Cuba. The aim of the project is to measure the target and projectile differential fragmentation cross sections in the energy range for PT (150-400 MeV/u) and RPS (up to 800 MeV/u) in order to improve the TPS and to develop a suitable spacecraft shielding for the future space missions. Different studies pointed out the need for a better description of the fragmentation effects in the current TPS to reach a greater accuracy in radiotherapy applications [32, 34]. Using the FOOT experiment data as a benchmark for the current MC simulation tools, it will be possible to improve the current nuclear interaction models allowing to benefit also other fields of physics.

In details, the main goal of the experiment is to measure target differential cross sections in energy (dσ/dE) with an accuracy of about 10% and projectile double differential

cross section in energy and angle ($d^2\sigma/d\Omega \cdot dE$) with an accuracy of about 5%. For the study of fragmentation cross sections, the targets of main interest are among the most abundant elements in the human tissues: ^1H, ^{12}C and ^{16}O, while ^{12}C, ^{16}O and ^4He are chosen for the beams.

In proton treatments, fragments are emitted along the beam path and they have short range, of the order of 10-100 μm, and low energy, $\sim$ MeV. Then, their probability of escaping the target is low. Even very thin targets would stop the particles or spoil the energy measurement. Target fragmentation cross sections will be hence measured using an inverse kinematic approach, studying the interactions using beams of ^{12}C and ^{16}O impinging on targets of graphite (C), hydrogenated target (polyethylene C_2H_4) and PMMA ($C_5O_2H_8$). The p-N cross sections are obtained by means of a stoichiometric subtraction method [35], e.g.

$$\sigma(\mathrm{H}) = \frac{1}{4}\Big(\sigma(\mathrm{C_2H_4}) - 2\sigma(\mathrm{C})\Big) \tag{2.1}$$

The same apparatus is employed to investigate the double differential cross sections of the projectile fragmentation process for beams of ^{12}C, ^{16}O and ^4He with kinetic energies in the range 100-400 MeV/u. In this case, fragments are produced with almost the same velocity of the primary beam and they are emitted from the target without relevant energy loss.

2.2.1 Experimental requirements

In order to match the precision requirements on the final cross section measurements deriving from radiobiological desiderata for PT, the FOOT experiment needs to achieve the following experimental resolutions:

- σ(p)/p $\sim 5\%$
- σ(TOF) $\sim$ 200 ps
- $\sigma(E_{kin})/E_{kin} \sim 2\%$
- $\sigma(\Delta\mathrm{E})/\Delta\mathrm{E} \sim 5\%$

where p is the momentum, TOF is the Time-Of-Flight, E_{kin} is the kinetic energy and ΔE is the energy loss.

2.3 Experimental setup

The FOOT project includes two alternative experimental setups. One is a magnetic spectrometer optimized for the identification of fragments with charge $Z \geq 3$ and an angular acceptance of about 10°. The other is an emulsion spectrometer for the tracking of low Z particles ($Z \leq 3$) and with an angular acceptance of about 70°. In both cases, the experimental setup includes an upstream region composed of two pre-target detectors to measure the impinging beam particles.

2.3.1 The Upstream Region

The detectors in the upstream region are adopted to measure the beam rate, the projectile direction and interaction point on the target. It is composed of the Start Counter (SC) plastic scintillator and the Beam Monitor (BM) drift chamber.

Start Counter
The SC is a plastic scintillator (EJ-228) [36] 250 μm thick. It provides the trigger for the acquisition system, it measures the incoming ion flux rate and, for the magnetic spectrometer, it provides also the start time for the Time-Of-Flight (TOF) measurement.

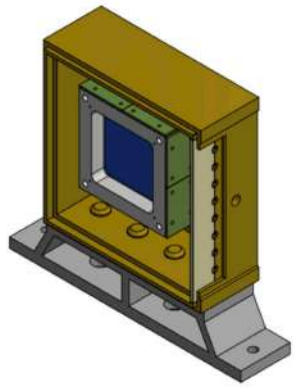

Figure 2.1: Start Counter detector inside the plastic box.

This detector consists of an active surface of 25 cm^2. It is supported by an aluminum frame enclosed in a black 3D-printed box to provide the necessary light tightness for the detector to function (Fig.2.1). 48 SiPMs are placed laterally to gather the light produced in the scintillator. The readout and powering of the SiPMs is handled by the WaveDAQ system [37]. The SC has been tested at CNAO (Italy) and GSI (Germany) with ^{12}C and ^{16}O ion beams at different energies. A time resolution of the order of 60 ps has been achieved for carbon ions at 700 MeV/u.

Beam Monitor
The BM is a drift chamber placed between the SC and the target. It measures the direction and the impinging point of the beam ions on the target. In addition, it is exploited to reject possible pre-target fragmentation events in the SC and in the BM itself.

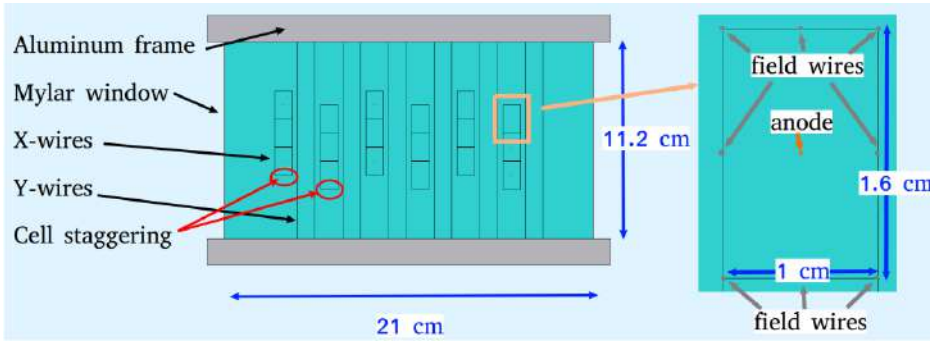

Figure 2.2: Sketch of the Beam Monitor drift chamber.

As shown in Fig.2.2, the BM detector consists of six layers of cells on each x and y view, with three rectangular drift cells (16 mm × 10 mm) per layer. To resolve left-right ambiguities in track reconstruction, two successive layers of the same view are staggered

by half a cell [38]. The BM active squared surface is of about 16 cm^2 and the total length is 21 cm. The efficiency and the spatial resolution of the detector have been studied at the Trento protontherapy facility with protons at 228 MeV and 80 MeV [39]. Values of about 90% and 100 μm have been found for the hit detection efficiency and the spatial resolution, respectively.

2.3.2 The Magnetic Spectrometer

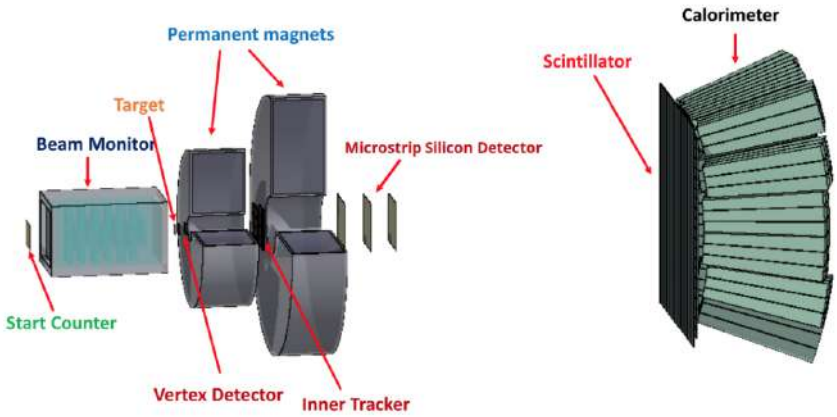

Figure 2.3: Schematic view of the magnetic spectrometer setup together with the upstream region.

The magnetic spectrometer has been optimized to measure heavy fragments and it is composed of different electronic detectors with a magnetic field required to detect the momentum of the beam particles. The overall apparatus size should lie within the 2–3 m range: the length of the setup changes according to the β of the beam to optimize the TOF resolution. The apparatus transversal dimension has been optimized by means of MC simulations to fit the heavy fragments angular distribution. Fig.2.3 shows a schematic view of the magnetic spectrometer setup, together with the upstream region. The magnetic spectrometer consists of an interaction and tracking region that is composed of the target, the Vertex detector (VT), the magnetic system, the Inner Tracker (IT) and the Microstrip Silicon Detector (MSD) (Fig.2.4). Then, there is a fragment identification region, located at least 1 m away from the target, which includes the Tof-Wall Detector (TW) and a Calorimeter (CA).

Vertex Detector
The VT is composed of four silicon pixel sensor layers of 2 × 2 cm^2 transverse dimension (Fig.2.5), placed along the direction of the incoming beam (z axis), guaranteeing a geometrical acceptance of about 40° for the emitted fragments. The layers are composed of MIMOSA-28 (M28) Monolithic Active Pixel Sensors (MAPS) which consist of a matrix with 928 (rows) × 960 (columns) pixels of 20.7 μm pitch. The VT detector is placed few millimeters beyond the target allowing a precise evaluation of the position where the projectile has interacted in the target originating the fragments [40].

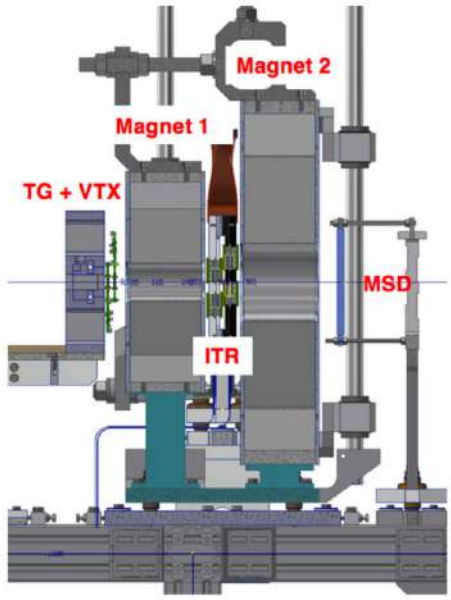

Figure 2.4: Interaction and Tracking region.

The Magnetic System
The magnetic system consists of two permanent magnets in Halbach configuration and it is employed to bend the fragments produced in the target in a direction orthogonal with respect to the beam direction. Two different magnet dimensions have been chosen to match the angular acceptance of 10° for the emitted fragments and to match the momentum resolution of $\sigma(p)/p \simeq 5\%$. The magnetic field profile along the beam line has two peaks with two maxima of 1.4 T and 0.9 T reached by the first (closest to the VT) and the second magnet, respectively.

Inner Tracker
The IT is made of two planes of M28 silicon pixel sensors to track the fragments in the magnetic region. Each plane is composed of two staggered ladders with four M28 sensors on each side supported by a metallic frame (Fig.2.6). The sensitive area covered by the planes is of about 64 cm^2.

Microstrip Silicon Detector
The MSD consists of three layers of silicon microstrip detectors. It is essential for the measurement of momentum and for the matching of the reconstructed tracks with the hits in the TW and in the Calorimeter, but it also provides a measurement of the fragments energy loss ΔE. The three layers are separated by a 2 cm gap and have an active area of 9.6 × 9.3 cm^2. Each MSD x-y layer contains two perpendicular Single-Sided Silicon Detector (SSSD) sensors glued on the two sides of a hybrid Printed Circuit Board (PCB) for mechanical support (Fig.3.6) and for providing the interface with the MSD readout [41]. The MSD is placed about 35 cm far from the target.

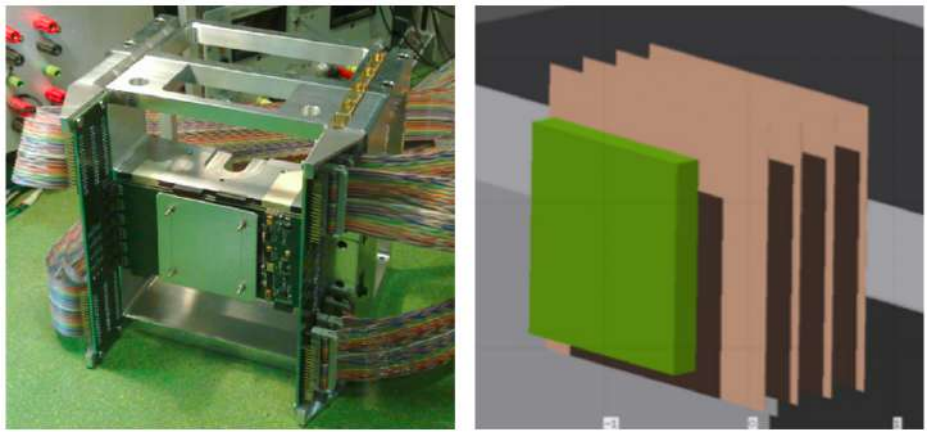

Figure 2.5: Target and Vertex detector setup.

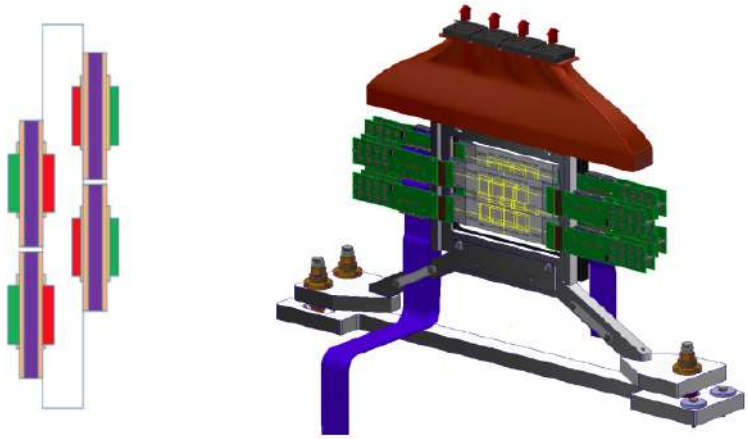

Figure 2.6: Inner Tracker from a perpendicular view (left) and along the beam axis (right).

Tof-Wall detector

The TW is composed of two layers of 20 orthogonally oriented plastic scintillator bars (EJ-200), 0.3 cm thick, 2 cm wide and 44 cm long, wrapped with reflective aluminum and darkening black tape to shield the material from background light sources [42] (Fig.2.8). The TW active surface is 40 × 40 cm^2 and has the purpose of measuring both the energy loss and the TOF, combined with the SC time measurement. These two values (dE/dx and TOF) allow to identify the charge Z of the impinging ions [43]. The thickness of the bars has been chosen to reach the FOOT requirements for the heavier fragments of a TOF resolution better than 100 ps and an energy loss resolution $\sigma(\Delta E)/\Delta E \simeq$ 3-10%. A TW energy loss resolution $\sigma(\Delta E)/\Delta E$ of about $6 - 14\%$ and a time resolution between $120 - 180$ ps have been obtained when the detector has been tested with proton beams. The same measures have been conducted with carbon ion beams at different energies and the results are $5 - 7\%$ and $30 - 40$ ps for energy loss and time resolution, respectively [44].

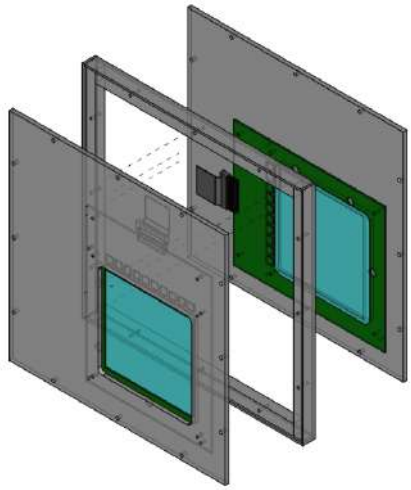

Figure 2.7: View of two layers of the MSD with sensors (blue) and PCB (green).

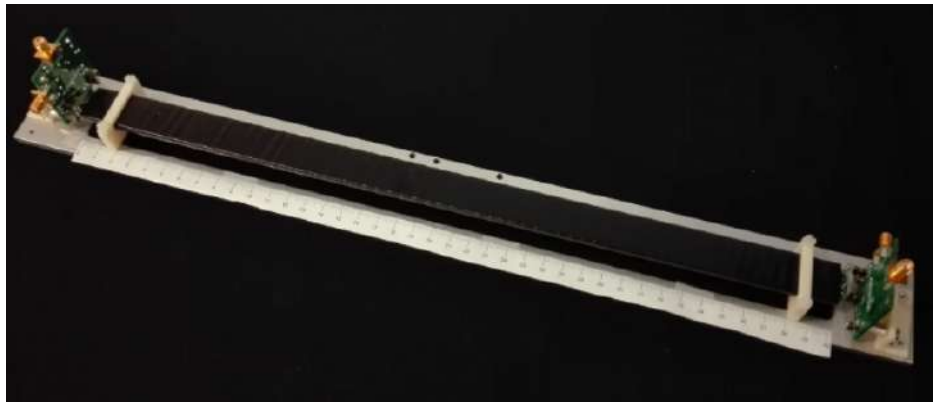

Figure 2.8: Picture of a plastic bar in the TW.

Calorimeter
The CA, the last downstream detector, is needed to measure the fragments kinetic energy in order to compute their mass. It is composed of 320 crystals of bismuth germanate (BGO) positioned with an approximately spherical arrangement ($\sim$ 20 cm radius), as shown in Fig.2.9. The crystals have an active surface of 2 × 2 cm^2 and they are grouped in Modules, i.e. matrices of 3 × 3 crystals [45]. The readout is based on SiPMs: each BGO crystal is coupled to a 25 SiPMs matrix. After different data takings conducted at CNAO and GSI with proton, helium, carbon and oxygen ion beams in the energy range of 70-400 MeV/u, the CA energy resolution $\sigma(\mathrm{E}_{kin})/\mathrm{E}_{kin}$ has been evaluated to be below 2% for the heavy particles ($Z \geq 3$).

2.3.3 The Emulsion Spectrometer

An emulsion spectrometer (ES) is employed to measure the differential cross sections of low Z fragments ($Z \leq 3$), which are produced with a large angular distribution. The

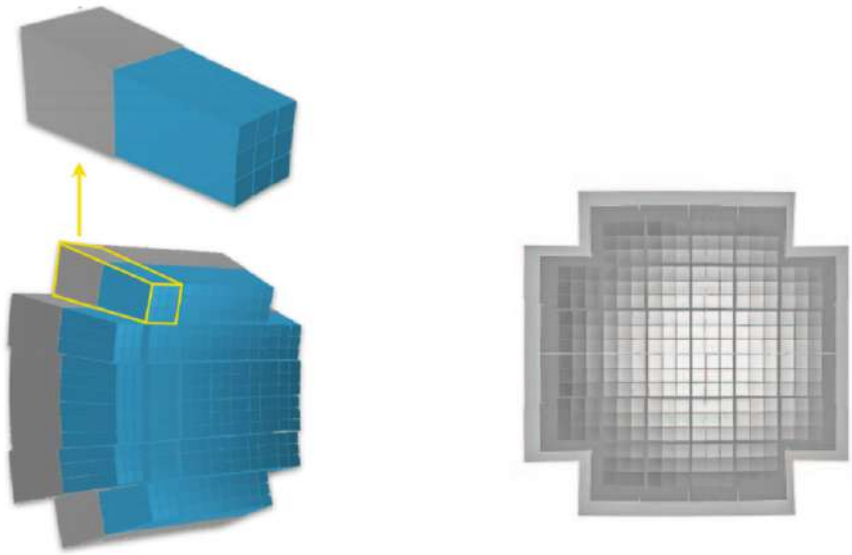

Figure 2.9: CA lateral view with zoom on a single Module (left) and CA front view (right).

ES, indeed, reaches an angular acceptance of about 70° with respect to the axis of the incident beam. The whole experimental setup consists of an upstream region, which includes the SC and the BM, followed by the ES, which is adopted to track and identify the fragments. The SC is employed to count the total number of delivered particles and to provide the trigger for the data acquisition, while the BM is adopted to measure the incident beam direction and the impinging point position on the ES. Counting the number of the delivered particles is needed because of the operating principle of the ES.

The ES is composed of different layers of emulsion films (detector) interleaved with passive material (target). The emulsion films are composed of two sensitive layers of gel with AgBr crystals deposited on the two side of a plastic base. The layer surface is of $12 \times 10\ cm^2$. When a charged particle crosses the emulsion, a sequence of AgBr crystals is sensitized along its trajectory, producing a latent image. After a chemical process known as development, the image turns into a sequence of black-silver grains. The 3-D position of the grains is obtained by means of an optical microscope. A particle track, with an associated volume and density, is reconstructed by considering all the aligned grains from all the layers of the consecutive emulsion films. The position resolution of the reconstructed track is of 0.3 μm. Since the density of a track is proportional to the ionization of the particle, a charge identification is allowed. Moreover, a refreshing procedure is adopted in order to overcome the saturation effect that occurs for highly ionizing particles. This procedure allows to extend the detector dynamical range by exploiting the oxidation of the latent image (fading) in order to erase the tracks of the less ionizing particles [46].

The processes taking place in the emulsion film when a beam crosses it makes the ES a one-shot detector: for each data taking, a different ES has to be assembled, exposed and lately analysed. The total number of delivered particles needs to be optimized because an excess of incident particles would increase the tracks pile-up worsening the reconstruction algorithm efficiency. On the other hand, an insufficiency in the number of particles would decrease the statistics not allowing a fully exploitation of the detector.

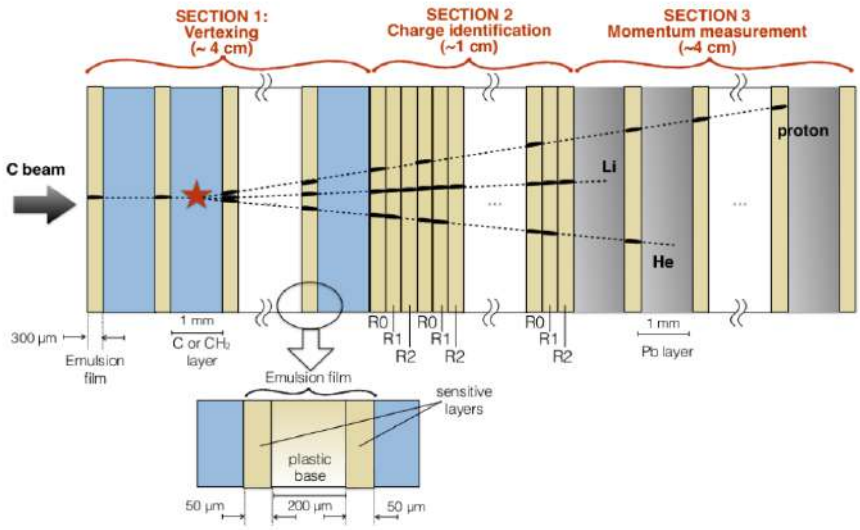

Figure 2.10: Scheme of ES structure.

The ES can be divided into three main sections (Fig.2.10):

- **Interaction and Vertexing**: this section contains several emulsion films interleaved with C or C_2H_4 target material layers. Secondary fragments are emitted when the beam interacts with the target material: the detector emulsion structure tracks the fragments and reconstructs the interaction vertex position.
- **Charge identification**: this section contains only emulsion films with the aim of reconstructing the fragments charge through the chemical processes of development and refreshing [47].
- **Energy and Mass Measurement**: this section contains emulsion films interleaved with layers of high Z material that can stop the particles in the detector. The aim is to measure the kinetic energy and the momentum of the beam particles that allow to identify the particle mass.

2.4 Charge and mass identification

In order to fulfill the FOOT expected performances presented in Sec.2.2.1, different particle identification (PID) techniques are exploited allowing also a redundancy in the measurement of the fragments mass. For the light fragments ($Z \leq 3$), the high tracking precision of the ES well satisfies all the required performances, as shown in [46]. Regarding the heavy fragments ($Z \geq 3$) detected by the magnetic spectrometer, the momentum p, the particle energy loss ΔE, the kinetic energy E_{kin} and the velocity β measurements are combined with different techniques to identify the charge and mass and to evaluate the double differential cross section.

Energy Loss ΔE
The ΔE is measured by the MSD and the TW detectors. The detectors performances,

characterized in different data takings, show a resolution of $\sigma(\Delta E)/\Delta E \sim 3 - 10\%$. In particular, the TW energy resolution can be modelled as:

$$\sigma(\Delta E) \sim a + \frac{b}{\Delta E}$$

where $a = 0.904\,\text{MeV}$ and $b = 18.6\,\text{MeV}$ [44].

Kinetic Energy E_{kin}
The E_{kin} is given by the sum of the energy depositions of the beam in the different detectors of the magnetic spectrometer. In particular, the main contribution to the measurement is given by the CA, whose resolution can be evaluated as:

$$\frac{\sigma(E_{kin})}{E_{kin}} = \frac{a}{\sqrt{E_{kin}}} \oplus \frac{b}{E_{kin}} \oplus c$$

where $a/\sqrt{E_{kin}}$ is a stochastic term, b/E_{kin} is given by the electronic noise of the readout and c is a constant contribution related to the calibration uncertainties. With the preliminary tests, a resolution of $\sigma(E_{kin})/E_{kin} \leq 2\%$ has been obtained for oxygen and carbon ion beams with kinetic energies of 80-400 MeV/u.

Velocity β
The particle velocity is evaluated with the following formula:

$$\beta = \frac{L}{c \cdot TOF} \tag{2.2}$$

where L is the fragment path length from the production position to the TW and TOF is the Time-Of-Flight measured by the SC and the TW. The L can be obtained with the global track reconstruction algorithm and its resolution is σ(L) $\sim$ mm. The TOF resolution, instead, is evaluated as $\sigma(\text{TOF}) = \sqrt{\sigma_{SC}^2 + \sigma_{TW}^2}$. The σ(TOF) reached by the preliminary tests is of about 70 ps for carbon and oxygen ions. Thus, the FOOT goal of σ(TOF) $\leq$100 ps for heavy fragments ($Z \geq 3$) is reached. The resolution of the particle velocity is given by $\sigma(\beta) \sim \frac{L}{c \cdot TOF^2} \cdot \sigma(TOF)$ and it is of the order of ~ 0.006.

Momentum p
Each detector of the magnetic spectrometer provides different hits that are elaborated by a global reconstruction algorithm. The latter allows the momentum evaluation. The preliminary tests show that the momentum resolution is $\sigma(p)/p \sim 5\%$

Charge Identification
In the magnetic spectrometer, the fragment charge can be evaluated with two different techniques. The first one involves the MSD and the TW detectors and consists in the estimate of the Bethe-Bloch energy loss formula shown in Eq.(1.1) that can be simplified as:

$$\frac{dE}{dx} \sim z^2 \cdot f(\beta) \tag{2.3}$$

where dE/dx is the energy loss, z is the particle charge and $f(\beta)$ is a function of the particle velocity β, which is expected to be similar to that of the primary particle. Both MSD and TW measure the energy release ΔE of the particle allowing an estimate of

the energy loss $\Delta E/\Delta x$, where Δx is the path length, which is considered almost equal to the detector thickness. The $\Delta E/\Delta x$ combined with the β measurement provides the charge identification.

The second technique involves the VT and the IT detectors. In particular, by crossing a layer of silicon pixel detector, a charged particle fires different adjacent pixels that can be grouped in a cluster. The cluster size, given by the number of fired pixels, depends on the particle energy loss and so on the incident particle charge. An empirical model has been developed to describe this dependence [40]:

$$n_p = 2\pi\, r_s\, \log\left(\frac{\Delta E}{2\pi E_g T_s}\right) \tag{2.4}$$

where n_p is the mean number of pixels, ΔE is the energy release, E_g is the mean energy for the creation of charge carriers (e.g. $E_g = 3.6\,\text{eV}$ for silicon material), T_s and r_s are two free parameters.

Combining Eq.(2.3) and Eq.(2.4), the particle charge can be extrapolated from the TOF measurement and the cluster size. By means of MC simulations, and given the ΔE resolution of the order of 3-10%, the fragment charge mis-identification level has been evaluated to be below 4%.

Mass Identification

The particle mass is evaluated combining the TOF, the momentum p and the E_{kin} measurements in three different ways:

- **TOF and momentum p:**

$$p = m\,\gamma\,\beta = \frac{m\,\beta}{\sqrt{1-\beta^2}} \;\Rightarrow\; m = \frac{p\sqrt{1-\beta^2}}{\beta}$$

$$A = \frac{m}{u} = \frac{1}{u}\frac{p\sqrt{1-\beta^2}}{\beta}$$

  where $u = 931.494\,\text{MeV}/c^2$ is the atomic mass unit, β is the particle velocity and γ is the Lorentz factor.

- **TOF and E_{kin}:**

$$p^2 = E_{tot}^2 - m^2 \quad\Rightarrow\quad m^2\,\gamma^2\,\beta^2 = (E_{kin}+m)^2 - m^2$$

$$A = \frac{m}{u} = \frac{E_{kin}}{u}\,\frac{1+\sqrt{1+\gamma^2\,\beta^2}}{\gamma^2\,\beta^2}$$

- **Momentum p and E_{kin}:**

$$E_{tot}^2 = p^2 + m^2 \quad\Rightarrow\quad (E_{kin}+m)^2 = p^2 + m^2$$

$$A = \frac{m}{u} = \frac{E_{kin}^2 - p^2}{2E_{kin}}$$

The three measurements will be combined with an Augmented Lagrangian Method and a standard χ^2 minimization algorithm. Preliminary results show the capability of the apparatus to disentangle the mass isotopes with the expected values of TOF, p and E_{kin}. However, the optimization of the mass reconstruction algorithm is still under study.

2.5 Simulation

MC simulations of the FOOT experiment are implemented with the purpose of optimizing the detector design and evaluating the expected performances. The FOOT simulation is performed by means of the FLUKA software: a MC simulation package for calculations of particle transport and interactions with matter [48, 49]. The experimental setup described in Sec.2.3 has been implemented in the MC simulation to properly take into account all the interactions of the particles with the whole FOOT apparatus. The simulations have been developed for different combinations of projectile species, beam kinetic energies and targets [50]. An example of a 2-D top view of the FOOT simulation setup is shown in Fig.2.11, in a geometrical configuration in which the distance between TG and TW is 1 m.

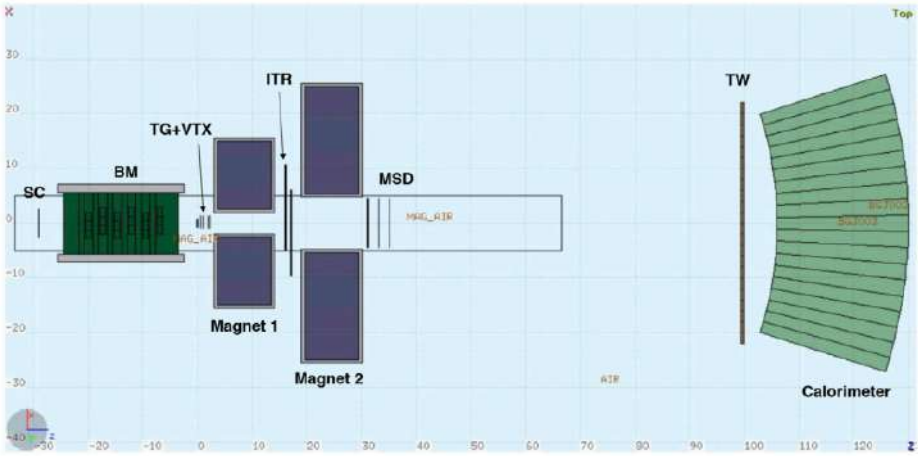

Figure 2.11: FLAIR visualization of the 2-D top view of the FOOT setup.

Charged particle transport is modeled in FLUKA through a multiple Coulomb scattering algorithm [51] based on the Molière theory. Hadron-nucleus interactions are modelled with the PEANUT (Pre-Equilibrium Approach to Nuclear Thermalization) model [52], which simulates the stages of INC and Pre-Equilibrium of nuclear interactions described in Sec.1.4 for particles with momenta below 5 GeV/c (energies relevant for the FOOT experiment). The Glauber-Gribov cascade model [53], instead, simulates the interactions for particles with momenta higher than 5 GeV/c. Nucleus-nucleus interactions are simulated in FLUKA with three different models depending on the energies involved: a Boltzmann-Master Equation model [28] for energy below 0.1 GeV/u, a relativistic Quantum Molecular Dynamics (rQMD) model [29] for energy between 0.1 and 5 GeV/u and a Dual Parton Model (DPM) and the Glauber theory are used with the DPMJET event generator [54] for energy higher than 5 GeV/u.

2.5.1 Fluka output

The MC code simulates the evolution of the primary particle and the other eventually produced particles event per event. The FOOT team modified the FLUKA code standard output developing a dedicated simulation output for the FOOT magnetic and emulsion spectrometers. In particular, an event per event data structure was included. The developed output of a FOOT simulation is an ASCII file which has been modeled on the

detectors characteristics, reproducing the information given by each of them in order to describe the whole history of the produced particles and to perform precise analysis of each event. Then, the ASCII file is converted into a ROOT file organized in three main blocks:

- **Particle block**: the kinematic information related to all the particles produced during the simulation is stored (e.g. particle mass, charge, position and momentum).
- **Detector block**: it stores each FOOT detector output, collecting all the relevant information (e.g. energy release, position and momentum values and all the quantity of interest for the specific detector). A pointer to the particle block is also saved.
- **Crossing block**: when a particle crosses a passive or active material defined in the FLUKA geometry, i.e. a region, the information about the crossing position and the particle momentum is stored, together with a pointer to the particle block.

2.6 Reconstruction

SHOE (Software for Hadrontherapy Optimization Experiment) is a ROOT based software developed within the FOOT collaboration for the track reconstruction and data analysis. It handles both MC and experimental data and it can be divided into three levels:

- **Local level**: to model and to reconstruct the relevant physics quantities of each detector of the experimental setup.
- **Global level**: to finalize the analysis combining the detectors information in order to reconstruct the global tracks information and to extract the fragment tracks and properties.
- **Analysis**: to evaluate the cross sections and the systematic errors starting from the reconstructed tracks.

At a Global level, the track reconstruction is performed by means of the GENFIT [55] software, which is a toolkit that performs track fitting. In GENFIT, the track fitting is based on three pillars: measurements, track representations and fitting algorithms. The latter comprises the Kalman filter, a reconstruction algorithm employed to reconstruct the track of each fragment in order to estimate the kinematics parameters of a specific particle.

Principle of Operation of Kalman Filters
In filtering algorithms, the track of a particle is considered as a dynamic system, described by a state vector. The Kalman filter is a recursive algorithm that finds the best estimate for the state of that dynamic system from a set of noisy measurements. It is a progressive method: the track parameter evaluation proceeds gradually including information of each additional measurement.

The evolution of a state vector $\bar{x}$ (the bar indicating the true value), which describes the track in each point of its trajectory, is represented by a system equation: $\bar{x}$ is extrapolated from the hit k - 1 to the hit k by means of the track model:

$$\bar{x}_k = f_k(\bar{x}_{k-1}) + w_{k-1} \tag{2.5}$$

where f_k is a state propagator (from hit k - 1 to hit k) and w_{k-1} designate random disturbances due to the process noise (e.g. multiple scattering or energy loss). The measured state vector m_k is the value of an observable measured by the k^{th} hit. m_k is a function of the state vector, with the addition of a measurement noise ϵ_k. The relation between m_k and $\bar{x}$ is the measurement equation:

$$m_k = h_k(\bar{x}_k) + \epsilon_k \tag{2.6}$$

In GENFIT, the state vector $\bar{x}$ is a 5-dimensional vector containing a track parametrization in plane coordinates: it specifies the particle charge over the momentum, the direction tangents and the position on the detector. Instead, m_k depends on detector type but generally it is a 3-dimensional vector containing hit coordinates. Given C_k the covariance matrix (error matrix) of $\bar{x}_k$, Q_k and V_k the covariance matrices of process and measurement noise w_k and ϵ_k respectively, the Kalman filter is a recursive algorithm that finds an estimate x_k for the unknown true state vector $\bar{x}$ of a system. The Kalman filter works in a two-step process: the prediction step and the update step. In the prediction step the algorithm produces estimates of the state vector, along with the uncertainties, from the measurements made at the (k - 1)th hit to the kth one. The state vector is indicated as x_k^{k-1}. In this step, also the covariance matrix C is predicted [56]. Then, in the update step, these estimates are updated considering the k^{th} hit information given by the measurement state m_k. All available information about x_k^{k-1} can be combined in a single χ^2 (between the predicted and measured state): minimizing it with respect to x_k, the update state vector becomes

$$x_k = x_k^{k-1} + K_k(m_k - h_k(x_k^{k-1})) \tag{2.7}$$

where $K_k = C_k H_k^T (V_k + H_k C_k H_k^T)^{-1}$ is the Kalman Gain Matrix, which depends on H_k, that is the projector matrix ($H_k \equiv \left(\frac{\partial h_k}{\partial x_k^{k-1}}\right)$), and on the covariance matrices C_k and V_k. K_k indicates how much the measurement suits the predicted state vector. A further step, the smoothing step [56], can be implemented to refine estimates of previous states going backward: it is a recursive operation which proceeds step by step in the direction opposite to that of the filtering (from k = n to k = 0). What described so far can be extended even to non-linear systems such as a charged particle trajectory in the FOOT magnetic field (Extended Kalman Filter).

The FOOT track Reconstruction algorithm

The FOOT reconstruction algorithm, which is based on the Kalman filter, takes as input the hit provided by each detector that is crossed by a particle in order to give as output a reconstructed global track. The presence of the hit on the TW is required to reconstruct a track because this detector provides the charge (see Sec.2.4) which is assigned to the track itself. If the track reconstruction is performed on a MC sample, each reconstructed track contains also all the relevant MC information, such as the association between the reconstructed track and the MC particles.

CHAPTER 3

Analysis

3.1 Introduction

The aim of this thesis is to evaluate the performances of the FOOT experiment track reconstruction algorithm. To reach this goal, a MC simulation with a primary beam of carbon ions with a kinetic energy of 200 MeV/u impinging on a carbon target has been performed by means of the FLUKA code. The analysis has been conducted with a MC simulation of 1M events considering the full setup of the FOOT experiment described in Sec.2.3. All the detector efficiencies and performances have been included in the simulation. Only the background noise, that depends on the environment in which a data taking is performed, has been neglected. Details about the MC simulations are presented in Sec.3.2. To study the performances of the Kalman filter, parameters such as efficiency, purity, momentum and angular resolution of the reconstruction algorithm have been evaluated and are presented in the following paragraphs.

3.2 Monte Carlo sample

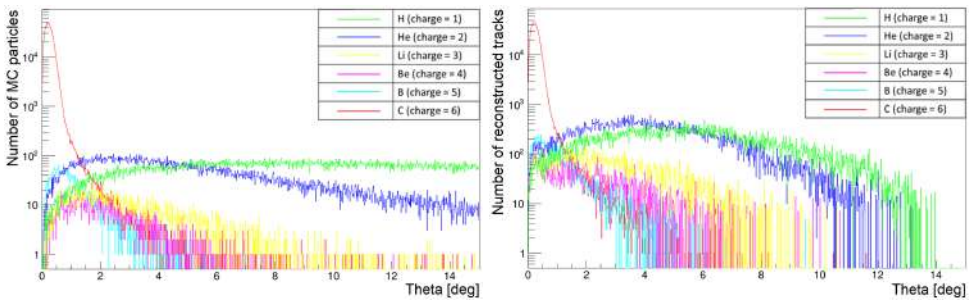

Figure 3.1: On the left: angular distribution of MC particles emitted from the target. On the right: angular distribution of reconstructed tracks with a reconstructed charge.

Fig.3.1 shows the angular distribution of MC particles emitted from the target and the angular distribution of the reconstructed tracks with the charge evaluated from the TOF and the ΔE measurements. As expected, the plot on the left shows that the angular distribution of light particles ($Z \leq 3$) is widely spread, while heavy fragments ($Z \geq 3$) are mainly emitted within a $\sim 10^{\circ}$ angle with respect to the initial projectile direction. The angular acceptance of the FOOT electronic setup ($\sim 10^{\circ}$) is shown in the figure on the right. In the same plot, the angular distribution of almost every charge shows a

peak within one degree on the x axis. Since MC light particles do not present any peak at low angles, the distribution of the reconstructed tracks has been re-evaluated using the charge of the MC particle which generated the highest number of hits in each track (Z true). For this reason, the plot has been redone and the output is shown in Fig.3.2. The peaks seen in Fig.3.1 are no longer present in Fig.3.2 and the angular distribution

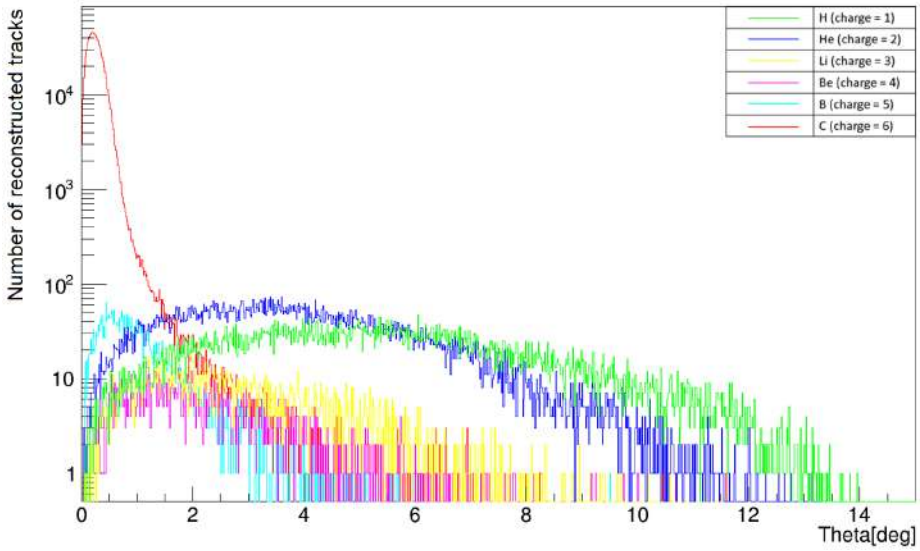

Figure 3.2: Angular distribution of reconstructed tracks. In this case the charge has been assigned by means of the MC information.

of reconstructed tracks matches that of MC particles. Those peaks are then the consequence of an incorrect evaluation of the charge of the global track caused by a charge mis-reconstruction in the TW detector or by secondary fragmentation.

For each reconstructed fragment, the MC information has been accessed to check whether the charge reconstructed in the TW was matching the true one. The result is shown in the so called *mixing* matrix of Fig.3.3 that compares the reconstructed charge (x axis) versus the true one (y axis). The non diagonal elements of the matrix indicate the number of mis-reconstructed charges for each fragment type. The misidentification is more relevant for particles with low charge. For example, particles with $Z_{true} = 1$ are identified as particles with $Z = 2$ (2% probability of misidentification), and particles with $Z_{true} = 2$ are identified as particles with $Z = 3$ (4% probability of misidentification). A possibility to mitigate the misidentification effect is to adopt an unfolding procedure [57].

There are cases, instead, where the TW correctly identifies the particle charge, but there is an incorrect evaluation of the charge of the global track due to secondary fragmentations. For example, if a particle undergoes a nuclear inelastic interaction in air shortly before the TW and one of the emitted secondary fragments maintains the direction of the initial particle, a global track can be reconstructed matching the hits of the two different particles and assigning the charge of the secondary fragment measured in the TW.

In order to study the secondary and the out-of-target fragmentation effects, the final position along the beam axis of the primaries is shown in Fig.3.4. Each peak in this plot corresponds to a specific detector component. For example, the first three peaks are the

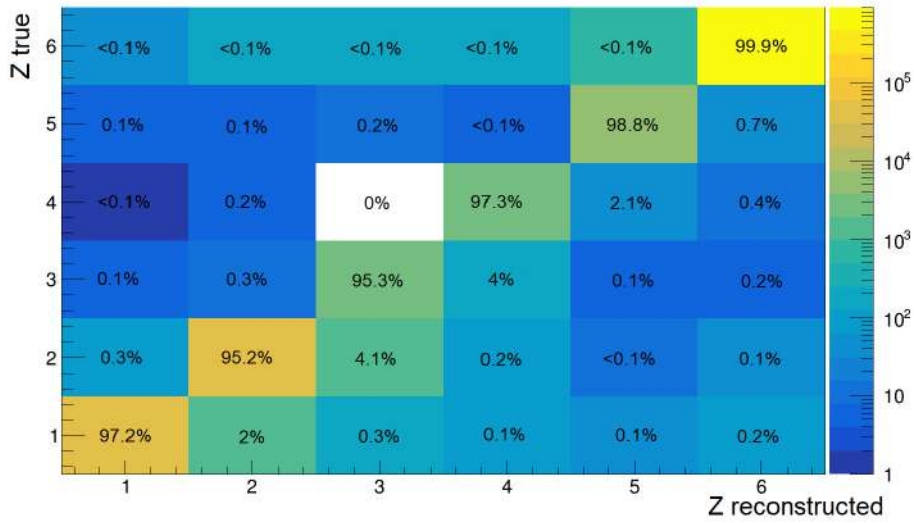

Figure 3.3: Correlation between the charge reconstructed by the TW (x axis) and the MC charge (y axis).

SC and the two BM mylar layers, while the peaks for $z > 0$ correspond to fragmentation in the other detectors along the experimental setup. To better study this phenomenon, an evaluation of the fragmentation rate of the primary in each detector has been conducted, as presented in Tab.3.1. Out-of-target and secondary fragmentation are not negligible. However, different methods to identify this background events are under study. For example, a possibility is to exploit the energy loss of the fragments measured in the different detectors and require their compatibility with the charge reconstructed in the TW.

Table 3.1: Primary beam fragmentation rate.

Region	Count of primary fragmentation	Percentage
Start Counter (SC)	1237	1.4%
Beam Monitor (BM)	1267	1.5%
Target	36442	42.4%
Vertex (VT)	1100	1.3%
Inner Tracker (IT)	5509	6.4%
Microstrip Silicon Detector (MSD)	7389	8.6%
Tof-Wall (TW)	28268	32.9%
Air	4761	5.5%

3.3 Efficiency

As described in Sec.2.6, the global reconstruction algorithm processes all the information from all the detectors (local level) to reconstruct the whole event (global level). It is then possible to evaluate its total efficiency and the efficiency of each detector. A count of the number of hits per detector per track has been conducted to evaluate the hit detection efficiency of each station of the FOOT tracking system. The result is shown in Fig.3.5 and

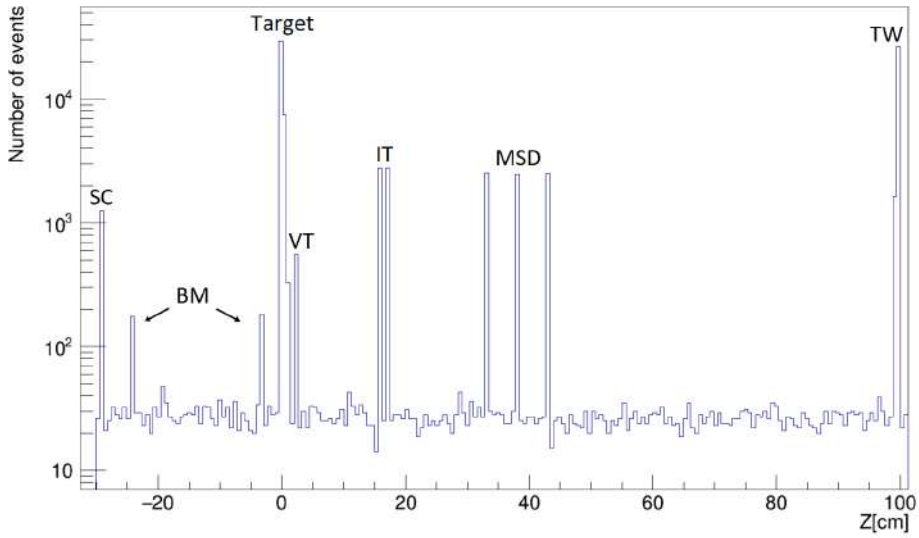

Figure 3.4: Position along the beam direction where the primary beam has a nuclear inelastic scattering.

3.6. The expected number of hits for the VT is four, which is the number of planes that

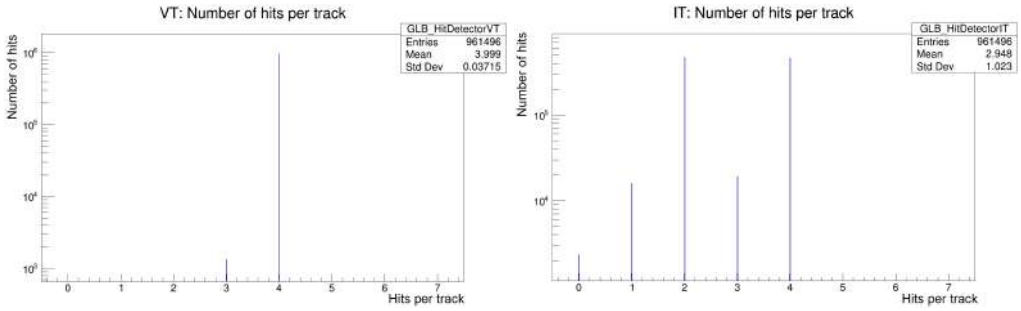

Figure 3.5: On the left: number of hits per track in the VT. On the right: number of hits per track in the IT.

constitute this detector. The efficiency of the VT is almost 1, hence the particle crosses all the four layers of silicon pixel sensors and it is correctly detected (Fig.3.5 on the left). For the IT, as shown in Fig.3.5 on the right, there are different peaks in the distribution of the number of hits. The cause is the geometry of the detector itself: the IT is composed of two staggered layers of silicon pixel detectors, each composed of two ladders with four M28 sensors on each side. When the particle crosses only one of the two ladders along the z axis because of their shift, the number of hits will be two instead of four. Moreover, the IT presents a dead area of $30\ \mu m$ between two consecutive sensors on the same ladder: if the particle crosses that area, it will not be detected. Since the MSD consists of three planes of silicon detectors, each one composed of two perpendicular layers of microstrip silicon sensors, the expected number of hits per track for this detector is six. Fig.3.6 shows some inefficiency effect that, however, can be neglected: the expected peak is about two orders of magnitude greater than the others shown.

The FOOT global track reconstruction algorithm efficiency has been evaluated con-

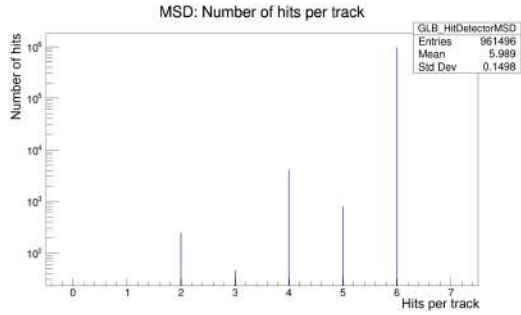

Figure 3.6: Number of hits per track in the MSD.

sidering the primary beam and the fragments produced in the target and impinging on the TW, taking into account the geometrical acceptance of the FOOT apparatus. The evaluation is then conducted on clean events: background events with a nuclear inelastic interaction of the projectile in the detectors before the target (in the SC or the BM), are neglected. To remove the effects of misidentification of the charge measured in the TW, the charge of the MC particle associated to the reconstructed track has been employed. For each charge with $1 \leq Z \leq 6$, the efficiency has been evaluated as the ratio between the total number of reconstructed tracks associated to a MC particle with a given charge and the total number of MC particles with the same charge emitted from the target and impinging on the TW:

$$Eff_i = \frac{\text{Number of reconstructed tracks}}{\text{Number of MC particles}} \tag{3.1}$$

Tab.3.2 shows the efficiency of the track reconstruction algorithm divided by charge.

Table 3.2: Efficiency of the track reconstruction algorithm.

Charge	Efficiency	Error
Z = 1	0.384	0.003
Z = 2	0.545	0.003
Z = 3	0.674	0.008
Z = 4	0.76	0.01
Z = 5	0.903	0.005
Z = 6	0.9685	0.0004

The highest values are achieved by the heavy fragments ($Z \geq 3$) and this result is in line with the goal of the experimental setup: the magnetic spectrometer is designed for the detection of heavy fragments. One of the aspects currently under study is the optimization of the parameters of the track reconstruction (e.g. minimum number of hits) in order to improve the efficiency results.

3.4 Purity

As for the efficiency study, also in this case a clean MC sample has been selected requiring that the MC particles are produced in the target and impinge on the TW. Each reconstructed track is composed of different hits which can be associated to different MC

particles. The purity of the track reconstruction algorithm has been evaluated calculating the ratio between the number of hits belonging to the particle to which the track has been assigned (MC particle which did the highest number of hits) and the total number of hits composing the given track:

$$Purity = \frac{\text{Number of hits of the main MC particle associated to the track}}{\text{Total number of hits of the track}} \tag{3.2}$$

The overall purity of the reconstruction algorithm is the mean value computed from all the results obtained for each track with eq.(3.2), and the result is shown in Tab.3.3. For each type of fragment, the purity is over 95%, meaning that the contamination of

Table 3.3: Purity of the track reconstruction algorithm.

Charge	Purity	Error
Z = 1	0.9780	0.0012
Z = 2	0.979	0.0010
Z = 3	0.981	0.002
Z = 4	0.973	0.003
Z = 5	0.952	0.003
Z = 6	0.99798	0.00005

different particles in the same reconstructed track is at a negligible level.

3.5 Momentum resolution

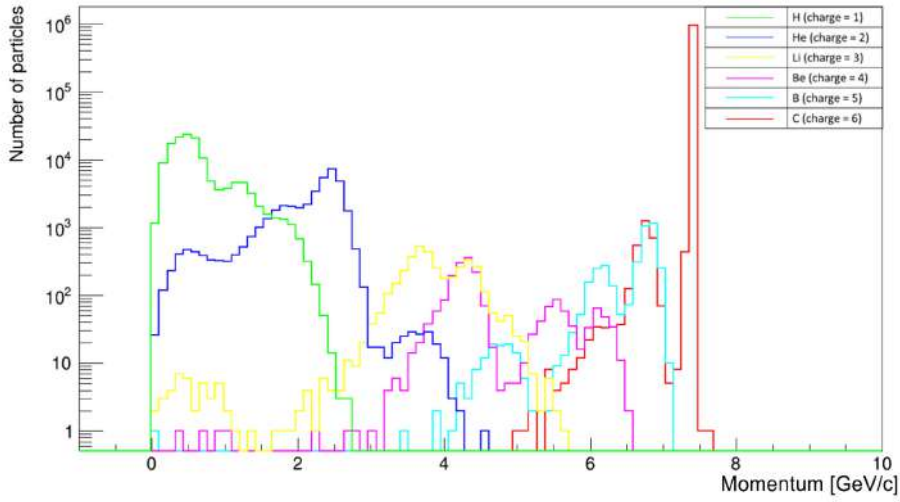

Figure 3.7: Momentum distribution of MC particles exiting the target as a function of the charge.

As illustrated in Sec.2.4, one of the FOOT experimental requirements is the reconstruction of the momentum p of the fragments to allow their mass identification. Fig.3.7 shows the momentum distribution of primary beam and secondary fragments exiting the target evaluated from the MC information. The upper limit of 8 GeV/c is reached by

the primary beam of carbon ions with a kinetic energy of 200 MeV/u. In the momentum spectra all the distributions show different peaks due to the contribution of the particle isotopes.

To fulfill the FOOT precision requirements on the final cross section measurements, a momentum resolution of about 5% needs to be achieved. The momentum resolution has been evaluated firstly as a function of the charge and then as a function of the charge and of the momentum. In order to avoid the contribution of the TW charge misidentification and the secondary fragmentation effects, the charge of the reconstructed track has been assigned accessing the MC information. In the first case, the resolution has been computed as the difference between the reconstructed track momentum and the MC one, both calculated at the exit of the target:

$$\sigma(p) = p_{reco} - p_{mc} \tag{3.3}$$

The evaluation has been conducted for all the particles with $1 \leq Z \leq 6$. Then, all the momentum resolution distributions have been fitted with a Gaussian. The standard deviation of the Gaussian represents the momentum resolution of a reconstructed track with a given charge. The results are shown in Fig.3.8, 3.9 and 3.10.

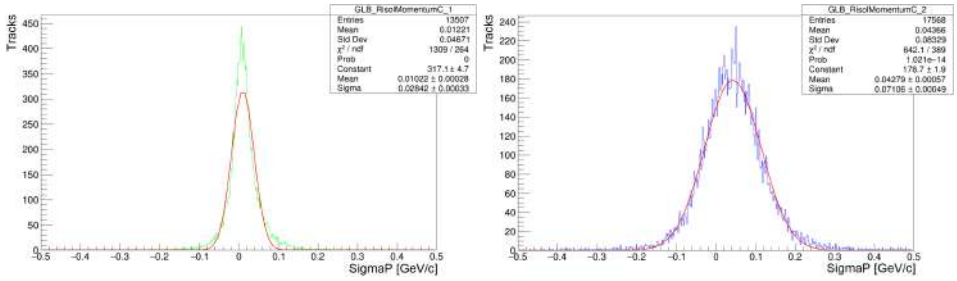

Figure 3.8: On the left: σ(p) for particles with charge $Z = 1$ (H). On the right: σ(p) for particles with charge $Z = 2$ (He).

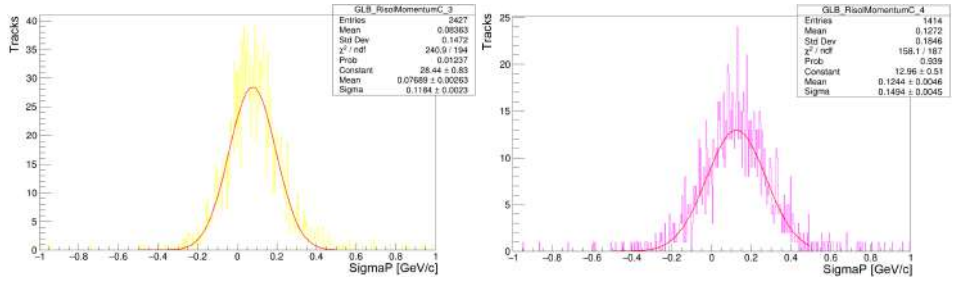

Figure 3.9: On the left: σ(p) for particles with charge $Z = 3$ (Li). On the right: σ(p) for particles with charge $Z = 4$ (Be).

In order to evaluate the momentum resolution as a function of the charge and of the momentum, the $\sigma(p)/p$ has been computed for each charge as the difference between the reconstructed track momentum and the MC one, divided by the MC momentum:

$$\sigma(p)/p = \frac{p_{reco} - p_{mc}}{p_{mc}} \tag{3.4}$$

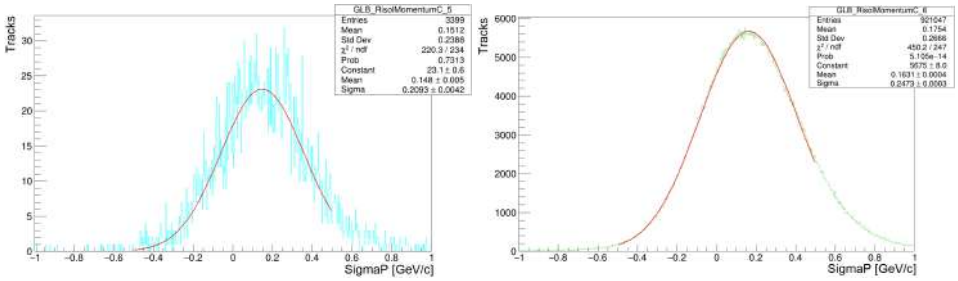

Figure 3.10: On the left: σ(p) for particles with charge $Z = 5$ (B). On the right: σ(p) for particles with charge $Z = 6$ (C).

The $\sigma(p)/p$ evaluation has been conducted starting from the $\sigma(p)$ divided by charge and then dividing it by momentum with a momentum range of 200 MeV/c. Examples of $\sigma(p)/p$ distributions are shown in Fig.3.11, 3.12 and 3.13.

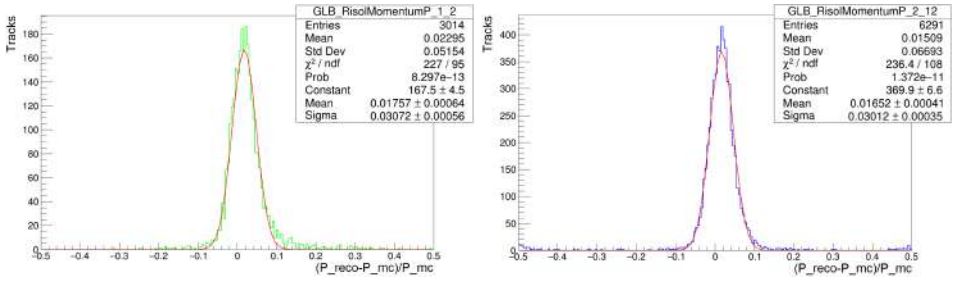

Figure 3.11: On the left: $\sigma(p)/p$ for particles with charge $Z = 1$ (H) in the range 200-400 MeV/c. On the right: $\sigma(p)/p$ for particles with charge $Z = 2$ (He) in the range 2200-2400 MeV/c.

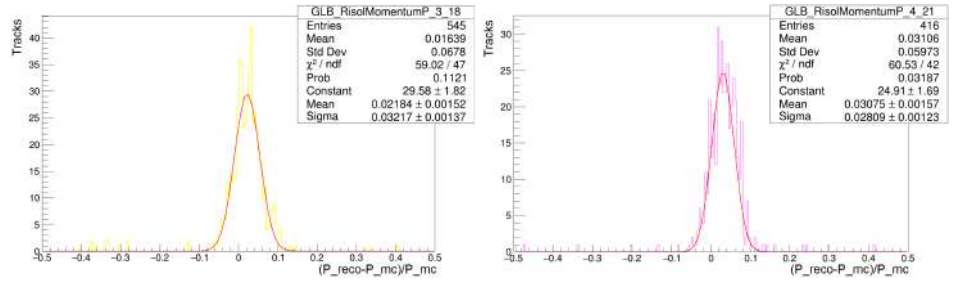

Figure 3.12: On the left: $\sigma(p)/p$ for particles with charge $Z = 3$ (Li) in the range 3400-3600 MeV/c. On the right: $\sigma(p)/p$ for particles with charge $Z = 4$ (Be) in the range 4000-4200 MeV/c.

All the $\sigma(p)/p$ plots are then fitted using a Gaussian function whose standard deviation σ represents the momentum resolution adopted to fill the total $\sigma(p)/p$ plot shown in Fig.3.14. The FOOT experiment required precision on the momentum measurement of about 5% is fulfilled for all the particle species. It has to be noticed that all the momentum resolution plots are not centered in zero, but there is a shift of the peak towards the positive direction of the x axis, meaning the presence of a systematic overestimate of the reconstructed momentum with respect to the MC value. This phenomenon is shown in

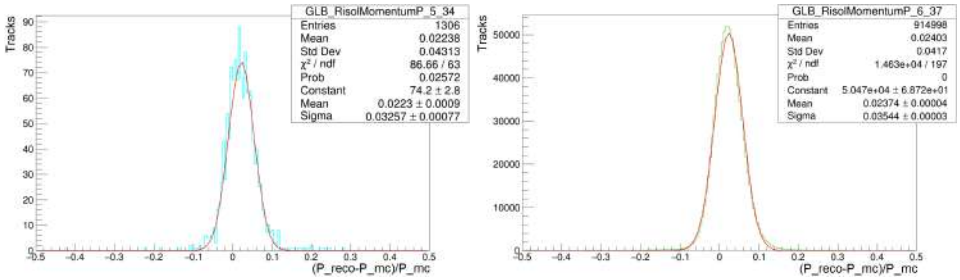

Figure 3.13: On the left: $\sigma(p)/p$ for particles with charge $Z = 5$ (B) in the range 6600-6800 MeV/c. On the right: $\sigma(p)/p$ for particles with charge $Z = 6$ (C) in the range 7200-7400 MeV/c.

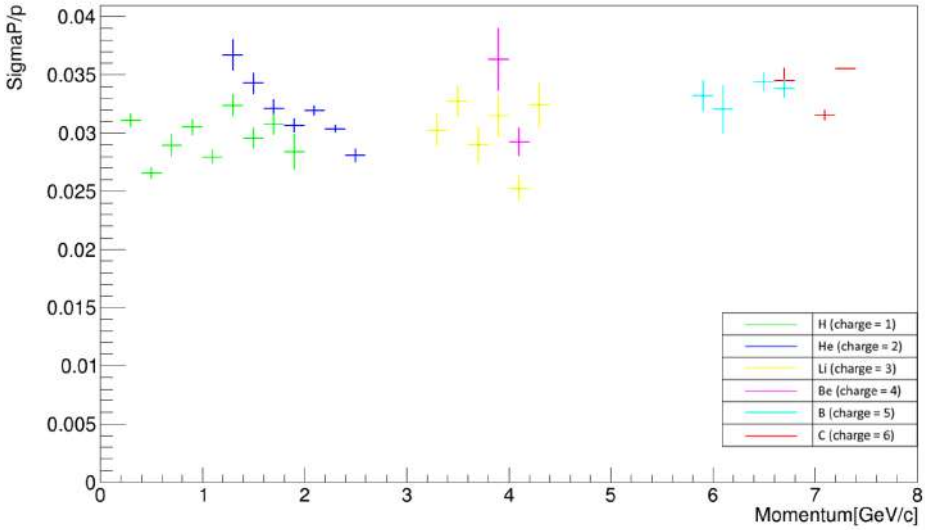

Figure 3.14: Momentum resolution as a function of the momentum.

Fig.3.15, where the mean of each of the Gaussian fit of the $\sigma(p)/p$ distributions is plotted as a function of the MC momentum. The shift is systematic and is of the order of 3%. The causes of it are currently under study.

3.6 Angular resolution

A procedure similar to the momentum resolution study has been followed to evaluate the angular resolution, firstly only dividing by charge and then dividing by charge and by momentum with a momentum range of 200 MeV/c. Also in this case, the reconstructed track charge has been assigned accessing the MC information. The angular resolution has been computed as the difference between the angle of emission from the target of the reconstructed particles and the MC one.

$$\sigma(\theta) = \theta_{reco} - \theta_{mc} \tag{3.5}$$

Fig.3.16, 3.17 and 3.18 show the angular resolution as a function of the charge, while Fig.3.19, 3.20 and 3.21 show some examples of angular resolution as a function of the

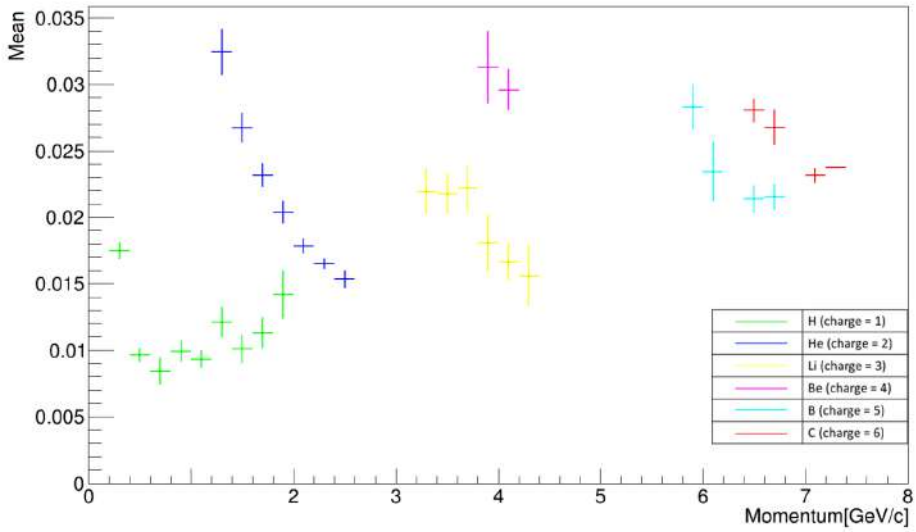

Figure 3.15: Mean of the Gaussian fit of the σ(p)/p plots as a function of the momentum.

charge and of the momentum for the particles with $1 \leq Z \leq 6$. All the $\sigma(\theta)$ plots are then fitted using a Gaussian function whose standard deviation σ represents the angular resolution adopted to fill the total $\sigma(\theta)$ plot shown in Fig.3.22. The angular resolution is of about $0.05°$ for the heavy fragments ($Z \geq 3$), while is up to $0.08°$ for the light ones. These results will contribute to the evaluation of the angular differential cross sections.

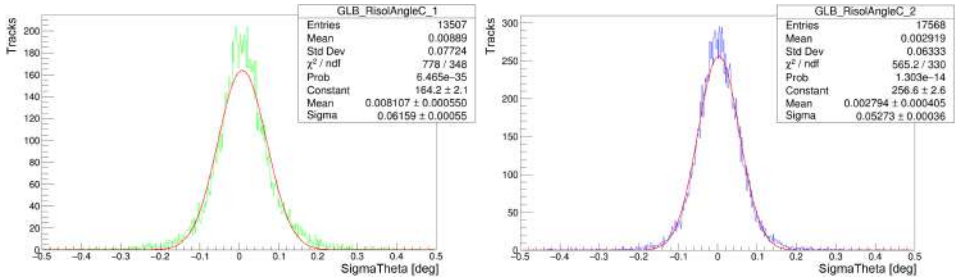

Figure 3.16: On the left: $\sigma(\theta)$ for particles with charge $Z = 1$ (H). On the right: $\sigma(\theta)$ for particles with charge $Z = 2$ (He).

Differently with respect to the momentum resolution evaluation, for the heavy fragments ($Z \geq 3$) the angular resolution plots do not show a shift on the x axis and the reconstructed angle matches the MC one. This effect can be observed also in Fig.3.23, where the mean of each Gaussian of the $\sigma\theta$ plots as a function of the momentum is plotted and almost all the values are centered in zero. However, the result of the angular resolution for the light fragments ($Z < 3$) is currently under study because the plots show a systematic shift of the order of $0.02°$ instead of being centered in zero.

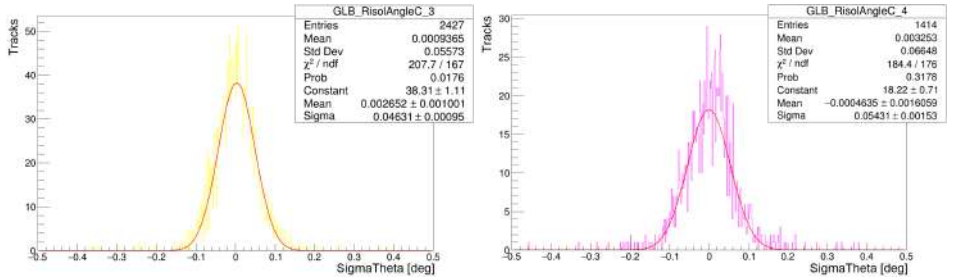

Figure 3.17: On the left: $\sigma(\theta)$ for particles with charge $Z = 3$ (Li). On the right: $\sigma(\theta)$ for particles with charge $Z = 4$ (Be).

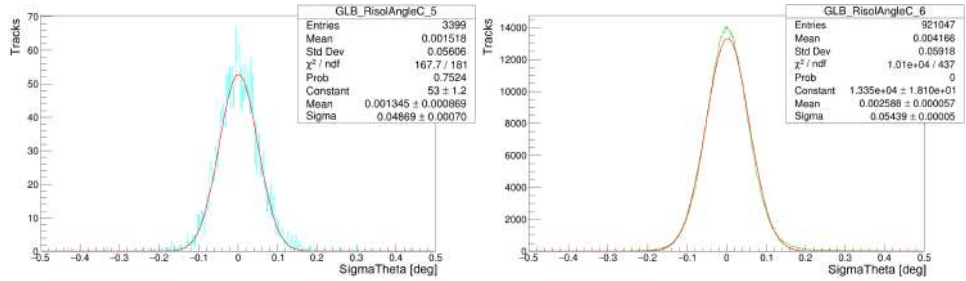

Figure 3.18: On the left: $\sigma(\theta)$ for particles with charge $Z = 5$ (B). On the right: $\sigma(\theta)$ for particles with charge $Z = 6$ (C).

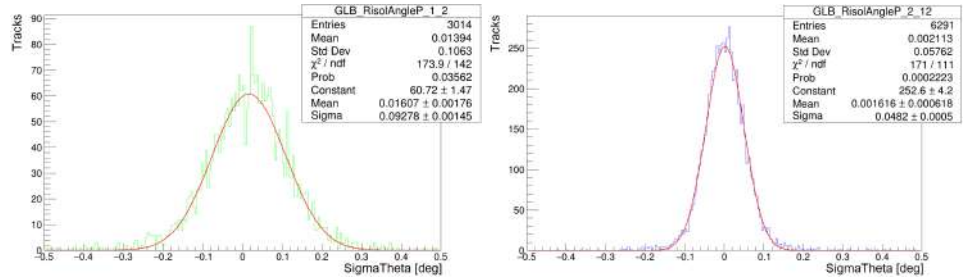

Figure 3.19: On the left: $\sigma(\theta)$ for particles with charge $Z = 1$ (H) as a function of the momentum in the range 200-400 MeV/c. On the right: $\sigma(\theta)$ for particles with charge $Z = 2$ (He) as a function of the momentum in the range 2200-2400 MeV/c.

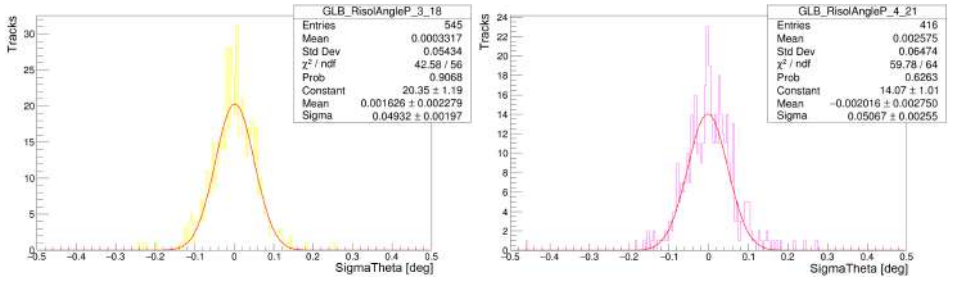

Figure 3.20: On the left: $\sigma(\theta)$ for particles with charge $Z = 3$ (Li) as a function of the momentum in the range 3400-3600 MeV/c. On the right: $\sigma(\theta)$ for particles with charge $Z = 4$ (Be) as a function of the momentum in the range 4000-4200 MeV/c.

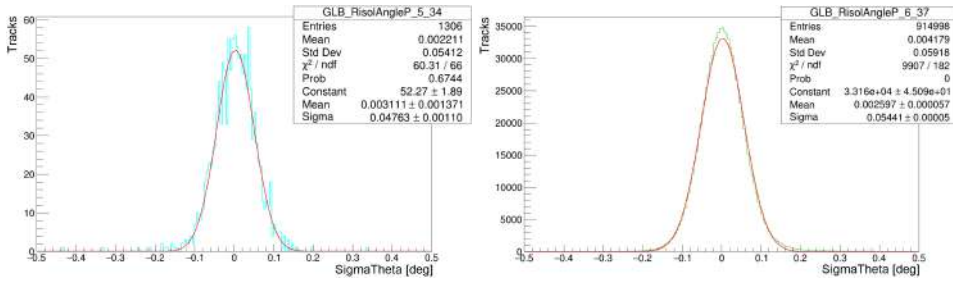

Figure 3.21: On the left: $\sigma(\theta)$ for particles with charge $Z = 5$ (B) as a function of the momentum in the range 6600-6800 MeV/c. On the right: $\sigma(\theta)$ for particles with charge $Z = 6$ (C) as a function of the momentum in the range 7200-7400 MeV/c.

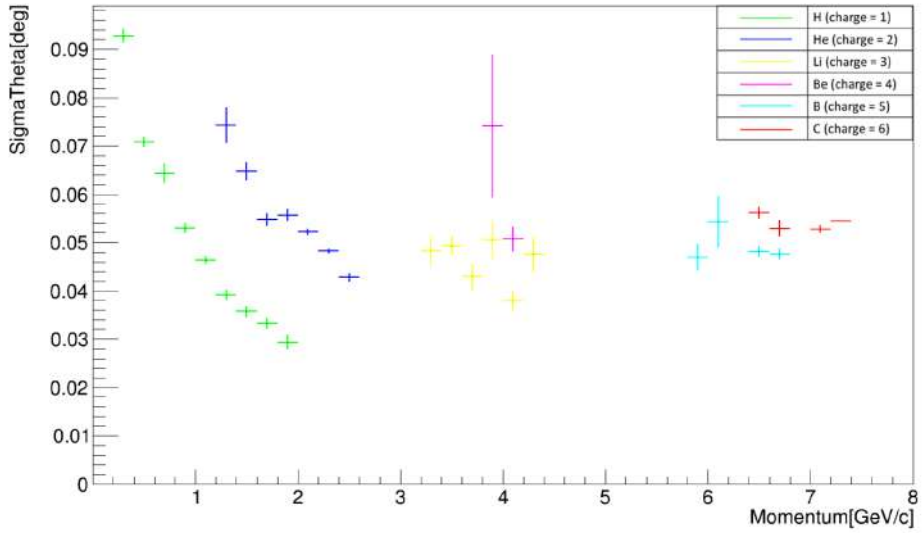

Figure 3.22: Angular resolution as a function of the momentum.

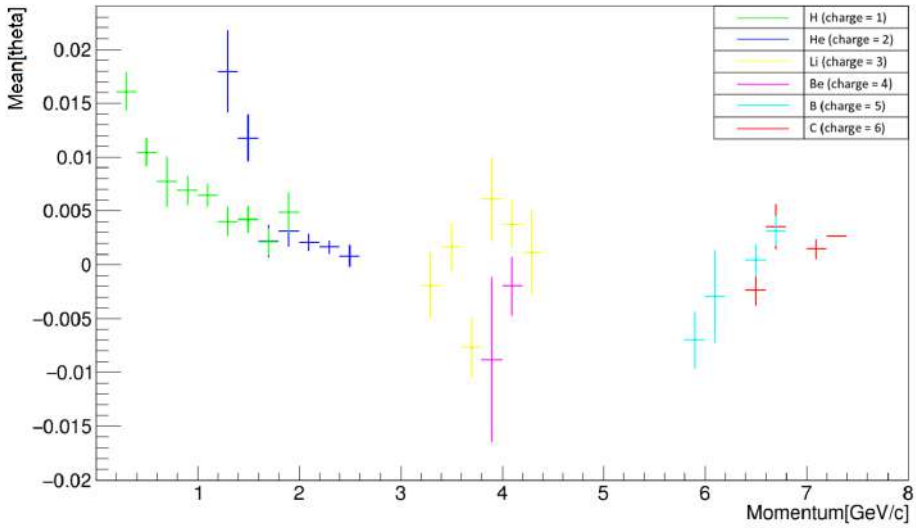

Figure 3.23: Mean of the Gaussian fit of the $\sigma(\theta)$ plots as a function of the momentum.

Conclusions

The FOOT (FragmentatiOn Of Target) collaboration designed an experiment to measure the nuclear target fragmentation differential cross sections in energy (dσ/dE) and the projectile double differential cross sections in energy and angle (d$^2\sigma$/dΩ·dE) of the particles (H, ^{12}C and ^{16}O) on the targets (C, polyethylene and PMMA) at the energies (100-800 MeV/u) of interest for particle therapy and radioprotection in space. The goal of the project is to fill the current lack of experimental data and to use the results as benchmark for the current MC simulation tools. The FOOT experiment includes two alternative setups: one with an emulsion spectrometer for the identification of light fragments ($Z \leq 3$) and the other with a magnetic spectrometer optimized for the identification of high Z ones ($Z \geq 3$). The latter, which is the one taken into account in this thesis, consists of different electronic detectors adopted to measure the particle time of flight, momentum, energy loss and kinetic energy. The charge identification is conducted with the time of flight and the energy loss measurements. The mass identification is performed combining the time of flight, the momentum and the kinetic energy measurements.

The aim of this thesis is to study and evaluate the performances of the FOOT experiment track reconstruction algorithm adopted to reconstruct the particle track and momentum. The study has been conducted with a MC simulation with a primary beam of carbon ions with a kinetic energy of $200MeV/u$ impinging on a carbon target. The simulation sample has been processed by the FOOT global reconstruction algorithm to include all the detectors efficiencies and resolution effects.

Firstly, a comparison between the angular distributions of MC particles and of reconstructed tracks has been conducted, showing an inconsistency at low angles for light fragments. In order to disentangle the track reconstruction performances with the charge identification efficiencies, the angular distribution of the reconstructed tracks has been re-evaluated assigning the charge by means of the MC information. In this case, the incongruity is no longer present and the angular distribution of the reconstructed tracks matches that of the MC particles.

Since both charge misidentification and secondary fragmentation effects can have an impact on the track reconstruction algorithm, a dedicated study has been conducted. Accessing the MC information, an evaluation of the probability of charge misidentification shows that particles with low charge ($Z \leq 3$) have more chance to be misidentified. For example, particles with $Z_{mc} = 1$ have a 2% chance of being identified as particles with $Z = 2$ and particles with $Z_{mc} = 2$ have a 4% chance of being identified as particles with $Z = 3$. Regarding the secondary fragmentation effect, an evaluation of the fragmentation rate of the primaries in each detector has been conducted. The result shows

that the out-of-target fragmentation rate is not negligible. Indeed, different techniques to identify this source of background are currently under study.

The second step of the analysis has been devoted to the evaluation of the efficiency of the track reconstruction algorithm. A count of the number of hits per detector per track has been conducted to evaluate the hit detection efficiency of each station of the FOOT tracking system. No relevant detectors inefficiencies have been shown. Then, the efficiency of the FOOT global track reconstruction algorithm has been evaluated, dividing the total number of reconstructed tracks by the total number of MC particles emitted from the target within the FOOT apparatus angular acceptance. The highest values are achieved by the heavy fragments ($Z \geq 3$). For example, the efficiency obtained for the carbon ion isotopes is $Eff = 0.9685 \pm 0.0004$. For the light fragments the efficiency is lower (e.g. $Eff = 0.674 \pm 0.008$ for lithium isotopes), but different optimization studies are ongoing to improve the current track reconstruction algorithm efficiency.

The evaluation of the purity has been conducted calculating the ratio between the number of hits belonging to the MC particle to which a given reconstructed track has been assigned and the total number of hits composing that track. A good result with a purity ≥ 0.95 has been obtained for all the particle species, with the highest value reached by the carbon isotopes (Purity$= 0.99798 \pm 0.00005$).

Finally, momentum and angular resolutions have been computed, firstly as a function of the charge and then as a function of the charge and of the momentum. The presence of a systematic overestimate of the reconstructed momentum with respect to the MC value has been observed. The shift is systematic of the order of 2-3% and the causes are currently under study. However, the FOOT required precision on the momentum measurement of about 5% is fulfilled for all the particle species. Differently from the momentum resolution evaluation, for the heavy fragments ($Z \geq 3$) the angular resolution does not show any systematic overestimate and the reconstructed angle matches the MC one. Instead, the results of the resolution for the light fragments are currently under study because they present a systematic shift of the order of $0.02°$. The angular resolution of the FOOT magnetic spectrometer is of about $0.05°$ for the heavy fragments ($Z \geq 3$) and of about $0.08°$ for the light fragments.

The results presented in this thesis showed the capability of the FOOT track reconstruction algorithm to fulfill the experimental requirements on the momentum and the angular resolutions. However, further studies are ongoing to improve the general performances of the algorithm, optimizing the track reconstruction parameters.

Bibliography

[1] Wu Hong-Gyun Park Jong Min, Kim Jung-in. Technological advances in charged-particle therapy. *Cancer Res Treat*, 53(3):635–640, 2021.

[2] Attix F.H. *Introduction to Radiological Physics and Radiation Dosimetry*. Wiley, 1986.

[3] Leo W.R. *Techniques for nuclear and particle physics experiments*. Springer-Verlag, 1987.

[4] M Inokuti and J E Turner. Mean excitation energies for stopping power as derived from oscillator-strength distributions. [review]. 1 1978.

[5] Barkas W.H. *Nuclear research emulsions. Vol.1: Techniques and theory*. Academic Press, 1963.

[6] M. Tanabashi, K. Hagiwara, and Hikasa et al. Review of particle physics, 34. passage of particles through matter. *Phys. Rev. D*, Aug 2022.

[7] Riccardo Ridolfi. *Adroterapia: principi e applicazioni*. PhD thesis, 09 2015.

[8] W. Ulmer. Theoretical aspects of energy range relations, stopping power and energy straggling of protons. *Radiation Physics and Chemistry*, 76(7):1089–1107, July 2007.

[9] Daniel Cussol. Hadron therapy. 09 2011.

[10] Bernard Gottschalk. Radiotherapy proton interactions in matter. 03 2018.

[11] Moliére G. Theorie der streuung schneller geladener teilchen ii. mehrfach- und vielfachstreuung. *Zeitschrift für Naturforschung A*, 3(2):78–97, 1948.

[12] Virgil L. Highland. Some practical remarks on multiple scattering. *Nuclear Instruments and Methods*, 129(2):497 – 499, 1975.

[13] Yung-Su Tsai. Pair production and bremsstrahlung of charged leptons. *Rev. Mod. Phys.*, 46:815–851, Oct 1974.

[14] Testa Mauro. *Charged particle therapy, ion range verification, prompt radiation*. Theses, Université Claude Bernard - Lyon I, October 2010.

[15] Martin Soukup, Matthias Fippel, and Markus Alber. A pencil beam algorithm for intensity modulated proton therapy derived from monte carlo simulations. *Physics in Medicine and Biology*, 50(21):5089–5104, oct 2005.

[16] Yupeng Li, Ronald X Zhu, Narayan Sahoo, Aman Anand, and Xiaodong Zhang. Beyond gaussians: a study of single-spot modeling for scanning proton dose calculation. *Physics in Medicine and Biology*, 57(4):983–997, feb 2012.

[17] Sebastian E. Kuhn and Gail E. Dodge. A fast algorithm for monte carlo simulations of multiple coulomb scattering. *Nuclear Instruments and Methods in Physics Research Section A: Accelerators, Spectrometers, Detectors and Associated Equipment*, 332(1):88 – 92, 1992.

[18] Francesco Tommasino, Emanuele Scifoni, and Marco Durante. New ions for therapy. *International Journal of Particle Therapy*, 2(3):428–438, 2015.

[19] Michael Joiner and Albert Van der Kogel. *Basic Clinical Radiobiology*. 03 2009.

[20] Marco Durante and Harald Paganetti. Nuclear physics in particle therapy: a review. *Reports on Progress in Physics*, 79(9):096702, aug 2016.

[21] Nadja Ebert, Falk Tillner, and Michael Baumann. Radiation oncology. In Paolo Boffetta and Pierre Hainaut, editors, *Encyclopedia of Cancer (Third Edition)*, pages 321–336. Academic Press, Oxford, third edition edition, 2019.

[22] Juliette Thariat, Samuel Valable, Carine Laurent, Siamak Haghdoost, Elodie A. Pérès, Myriam Bernaudin, François Sichel, Paul Lesueur, Mathieu Césaire, Edwige Petit, Aurélie E. Ferré, Yannick Saintigny, Sven Skog, Mihaela Tudor, Michael Gérard, Sebastien Thureau, Jean-Louis Habrand, Jacques Balosso, and François Chevalier. Hadrontherapy interactions in molecular and cellular biology. *International Journal of Molecular Sciences*, 21(1), 2020.

[23] Perez C.A. and Brady L.W. *Principles and Practice of Radiation Oncology*. Wolters Kluwer/Lippincott Williams Wilkins, Philadelphia, sixth edition edition, 2013.

[24] Aafke Christine Kraan. Range verification methods in particle therapy: Underlying physics and monte carlo modeling. *Frontiers in Oncology*, 5, 2015.

[25] M. Blann. Hybrid model for pre-equilibrium decay in nuclear reactions. *Phys. Rev. Lett.*, 27:337–340, Aug 1971.

[26] V. Weisskopf. Statistics and nuclear reactions. *Phys. Rev.*, 52:295–303, Aug 1937.

[27] Peter Fong. Statistical theory of nuclear fission: Asymmetric fission. *Phys. Rev.*, 102:434–448, Apr 1956.

[28] G. Battistoni et al. Heavy ion interactions from Coulomb barrier to few GeV/n: Boltzmann master equation theory and FLUKA code performances. *Braz. J. Phys.*, 34:897–900, 2004.

[29] The fluka code for space applications: recent developments. *Advances in Space Research*, 34(6):1302 – 1310, 2004. Space Life Sciences: Radiation Risk Assessment and Radiation Measurements in Low Earth Orbit.

[30] K Gunzert-Marx, H Iwase, D Schardt, and R S Simon. Secondary beam fragments produced by 200 MeV u-112c ions in water and their dose contributions in carbon ion radiotherapy. *New Journal of Physics*, 10(7):075003, jul 2008.

[31] Tommasino Francesco and Durante Marco. Proton radiobiology. *Cancers*, 7(1):353–381, 2015.

[32] Marco Durante and Francesco Tommasino. Proton radiobiology. *Cancers (Basel)*, 7, 02 2015.

[33] Giuseppe Battistoni, Marco Toppi, Vincenzo Patera, and The Collaboration. Measuring the impact of nuclear interaction in particle therapy and in radio protection in space: the foot experiment. *Frontiers in Physics*, 8, 02 2021.

[34] David Thwaites. Accuracy required and achievable in radiotherapy dosimetry: Have modern technology and techniques changed our views? *Journal of Physics Conference Series*, 444:2006–, 06 2013.

[35] J. Dudouet, D. Juliani, M. Labalme, D. Cussol, J. C. Angélique, B. Braunn, J. Colin, Ch. Finck, J. M. Fontbonne, H. Guérin, P. Henriquet, J. Krimmer, M. Rousseau, M. G. Saint-Laurent, and S. Salvador. Double-differential fragmentation cross-section measurements of 95 mev/nucleon ^{12}c beams on thin targets for hadron therapy. *Phys. Rev. C*, 88:024606, Aug 2013.

[36] R.A. Weldon, J.M. Mueller, P. Barbeau, and J. Mattingly. Measurement of ej-228

plastic scintillator proton light output using a coincident neutron scatter technique. *Nuclear Instruments and Methods in Physics Research Section A: Accelerators, Spectrometers, Detectors and Associated Equipment*, 953:163192, 2020.

[37] Marco Francesconi et al. The WaveDAQ integrated Trigger and Data Acquisition System for the MEG II experiment. 6 2018.

[38] Z Abou-Haidar, C Agodi, and M A G Alvarez et al. Performance of upstream interaction region detectors for the first experiment at gsi. *Journal of Instrumentation*, 7(02):P02006, feb 2012.

[39] Yunsheng Dong, Silvestre Gianluigi, and Colombi Sofia et al. The drift chamber detector of the foot experiment: Performance analysis and external calibration. *Nuclear Instruments and Methods in Physics Research Section A: Accelerators, Spectrometers, Detectors and Associated Equipment*, 986:164756, 2021.

[40] E. Spiriti, Ch. Finck, J. Baudot, C. Divay, D. Juliani, M. Labalme, M. Rousseau, S. Salvador, M. Vanstalle, C. Agodi, G. Cuttone, M. De Napoli, and F. Romano. Cmos active pixel sensors response to low energy light ions. *Nuclear Instruments and Methods in Physics Research Section A: Accelerators, Spectrometers, Detectors and Associated Equipment*, 875:35–40, 2017.

[41] Keida Kanxheri, Mattia Barbanera, Giovanni Ambrosi, Gianluigi Silvestre, Silvia Biondi, Riccardo Ridolfi, Martina Villa, D. Aisa, Mirco Caprai, M. Ionica, Pisana Placidi, and Leonello Servoli. The microstrip silicon detector (msd) data acquisition system architecture for the foot experiment. *Journal of Instrumentation*, 17:C03035, 03 2022.

[42] Eljen plastic scintillator. `https://eljentechnology.com/products/plastic-scintillators`. Accessed: 2020-08-06.

[43] A. C. Kraan et al. Charge identification performance of a Δ E-TOF detector prototype for the FOOT experiment. *Nucl. Instrum. Meth. A*, 958:162422, 2020.

[44] Matteo Morrocchi and Ciarrocchi et al. Development and characterization of a ΔE-TOF detector prototype for the FOOT experiment. *Nuclear Instruments and Methods in Physics Research A*, 916:116–124, February 2019.

[45] L. Scavarda. Design and performance of the Calorimeter for the FOOT experiment. *Nuovo Cim. C*, 43(4-5):123, 2020.

[46] M.C. Montesi et al. Ion charge separation with new generation of nuclear emulsion films. *Open Physics*, 17(1):233–240, 2019.

[47] Giuliana Galati and Andrey Alexandrov et al. Charge identification of fragments with the emulsion spectrometer of the foot experiment. *Open Physics*, 19(1):383–394, 2021.

[48] Alfredo Ferrari, Paola Sala, Alberto Fasso, and J. Ranft. Fluka: a multi-particle transport code. *CERN Yellow report*, 2005-10, 01 2005.

[49] G. Battistoni et al. The FLUKA Code: An Accurate Simulation Tool For Particle Therapy. *Front. Oncol.*, 6:116, 2016.

[50] T.T. Böhlen et al. The fluka code: Developments and challenges for high energy and medical applications. *Nuclear Data Sheets*, 120:211–214, 2014.

[51] A. Ferrari, P.R. Sala, R. Guaraldi, and F. Padoani. An improved multiple scattering model for charged particle transport. *Nuclear Instruments and Methods in Physics Research Section B: Beam Interactions with Materials and Atoms*, 71(4):412–426, 1992.

[52] `http://www.fluka.org/content/manuals/online/18.15.2.html`.

[53] R.J. Glauber and G. Matthiae. High-energy scattering of protons by nuclei. *Nuclear Physics B*, 21(2):135–157, 1970.

[54] Stefan Roesler, Ralph Engel, and Johannes Ranft. The Monte Carlo event generator DPMJET-III. In *International Conference on Advanced Monte Carlo for Radiation Physics, Particle Transport Simulation and Applications (MC 2000)*, pages 1033–1038, 12 2000.

[55] Johannes Rauch and Tobias Schlüter. Genfit — a generic track-fitting toolkit. *Journal of Physics: Conference Series*, 608(1):012042, apr 2015.

[56] `http://www-jlc.kek.jp/subg/offl/kaltest/`.

[57] Volker Blobel. An unfolding method for high energy physics experiments. 09 2002.